Journal of Nanomaterials

Nanostructured Thin Films and Coatings

Guest Editors: Ping Xiao and Robert Dorey

Nanostructured Thin Films and Coatings

Journal of Nanomaterials

Nanostructured Thin Films and Coatings

Guest Editors: Ping Xiao and Robert Dorey

Contents

Hindawi Publishing Corporation
Journal of Nanomaterials
Volume 2008, Article ID 931380, 2 pages
doi:10.1155/2008/931380

Editorial
Nanostructured Thin Films and Coatings

Ping Xiao[1] and Robert Dorey[2]

[1] *School of Materials, University of Manchester, Grosvenor Street, Manchester M1 7HS, UK*
[2] *School of Applied Sciences, Microsystems and Nanotechnology Centre, Cranfield University, Cranfield, Bedfordshire MK43 0AL, UK*

Correspondence should be addressed to Ping Xiao, ping.xiao@manchester.ac.uk

Received 1 April 2008; Accepted 1 April 2008

The field of films and coating continues to develop with new materials, processing, and applications being envisaged. This special edition of Journal of Nanomaterials examines some of the latest developments in nanostructured thin films and coatings. Nanostructured thin films and coatings possess properties different to homogenous materials due to the deliberate engineering of nanoscale features into the structure. The seven papers presented in this special edition examine the challenges faced in fabricating nanoscale systems and composites, as well as the electrical and light interactions that occur with such small-scale systems

In the first paper, glass plate-supported nanostructure ZnO thin films were deposited by sol-gel spin coatings. The ZnO thin films are transparent ca 80-90% in visible range, and have absorption edge at about 370 nm. The c-axis orientation improves and the grain size increases, which was indicated by an increase in intensity of the (002) peak at 34.40 in XRD corresponding to the hexagonal ZnO crystal. The photocatalytic degradation of X6G, an anionic monoazo dye, in aqueous solutions was investigated, and the effects of some operational parameters such as the number of layers and reusability of ZnO nanostructure thin film were examined. The results showed that the five-layer coated glass surfaces have a very high photocatalytic performance.

In the second paper, the microstructure and photocatalytic performance of titania coatings obtained by different thermal spray techniques were investigated: atmospheric plasma spraying (APS), suspension plasma spraying (SPS)—alternative plasma spray technique using liquid feedstock material and the high-velocity oxygen fuel spray process (HVOF). Various titania powders were used as feedstock materials for spraying. Different TiO_2 nanopowder suspensions were carried out to study the influence of the solvent nature on the coating characteristics. The photocatalytic efficiency of the elaborated samples was tested in an environmental test chamber setup and evaluated from the gaseous nitrogen oxide (NO, NOx) removal.

In the third paper, the structural, optical, and conductivity properties of silicon film deposited on cerium dioxide buffer layer were studied. The data of Raman scattering measurements, scanning electron microscopic experiments, and electrophysical measurements were used. The temperature spatial distribution and cerium dioxide phase conditions play a great role in silicon crystallization. Applied external electric field was used to destroy the crystal structure order in silicon. Crystal phase of silicon film was restored by annealing the samples. The field destruction of crystal phase and its restoration after annealing were investigated by Raman spectroscopy.

In the fourth paper, a study was concentrated on preparation and structural characterization of granular Ag-ZrO_2, Co-ZrO_2, and Au-ZrO_2 thin films grown by pulsed laser deposition (PLD) in a wide range of volume fraction x of metal ($0.08 < xAg < 0.28$, $0.06 < xCo < 0.40$, and $0.08 < xAu < 0.55$). High-resolution transmission electron microscopy (HRTEM) showed regular distribution of spherical Au, Co, and Au nanoparticles having very sharp interfaces with the amorphous matrix. The structural results are compared aiming to stress the effect of the actual microstructure on the percolation threshold. Two different mechanisms of particle growing as a function of the metal content are evidenced: nucleation and particle coalescence, with

their relative significance depending strongly on the type of metal, giving rise to very different values of the percolation threshold (xc(Ag)~0.28, xc(Co)~0.35, and xc(Au)~0.55).

In the fifth paper, inorganic thin films (hydroxide, oxide, and phosphate materials) that are textured on a submicron scale have been prepared from aqueous metal salt solutions at room temperature using vapor-diffusion catalysis. This generic synthesis approach mimics the essential advantages of the catalytic, and structure-directing mechanisms observed for the formation of silica skeletons of marine sponges. Chemical composition, crystallinity, and the three-dimensional morphology of thus prepared films are extremely sensitive to changes in the synthesis conditions, such as concentrations, reaction times and the presence and nature of substrate materials. Focusing on different materials systems, the reaction mechanism for the formation of these thin films and the influence of different reaction parameters on the product are explained.

In the sixth paper, chromium metal-induced nanocrystallization of amorphous silicon (a-Si) thin films is reported. The nanocrystalline nature of these films is confirmed from X-ray diffraction and Raman spectroscopy. Significantly, the deconvolution of Raman spectra reveals that the thin films were crystallized in a mixed phase of cubic diamond and wurzite structure as evidenced by the lines at 512 and 496 cm^{-1}, respectively. The crystallite sizes were between 4 and 8 nm. Optical properties of the crystallized silicon, derived from spectral transmittance curves, revealed high transmission in the region above the band gap. Optical band gap varied between 1.3 and 2.0 eV, depending on the nature of crystallinity of these films, and remained unaltered with an increase in Cr addition from 5 to 30%. This signifies that the electronic structure of the nanocrystalline silicon films is not affected considerably inspite of the presence of metal silicides and the process of crystallization.

In the final paper, the thermomechanical stresses acting between a nanotube and fullerenes encapsulated on it are computed. After a general formulation, based on elasticity, the analysis suggests that a thermal control could be used to produce smart fullerenes at nanotube systems, for example, as two-stage nanovectors for drug delivery.

Ping Xiao
Robert Dorey

Hindawi Publishing Corporation
Journal of Nanomaterials
Volume 2008, Article ID 356765, 5 pages
doi:10.1155/2008/356765

Research Article

Preparation of Glass Plate-Supported Nanostructure ZnO Thin Film Deposited by Sol-Gel Spin-Coating Technique and Its Photocatalytic Degradation to Monoazo Textile Dye

Mohammad Hossein Habibi and Mohammad Khaledi Sardashti

Catalysis Division, Department of Chemistry, University of Isfahan, Isfahan 81746-73441, Iran

Correspondence should be addressed to Mohammad Hossein Habibi, mhhabibi@yahoo.com

Received 9 July 2007; Accepted 8 January 2008

Recommended by Robert Dorey

Glass plate-supported nanostructure ZnO thin films were deposited by sol-gel spin coating. Films were preheated at 275°C for 10 minutes and annealed at 350, 450, and 550°C for 80 minutes. The ZnO thin films were transparent ca 80–90% in visible range and revealed that absorption edges at about 370 nm. The *c*-axis orientation improves and the grain size increases which was indicated by an increase in intensity of the (002) peak at 34.4° in XRD corresponding to the hexagonal ZnO crystal. The photocatalytic degradation of X6G an anionic monoazo dye, in aqueous solutions, was investigated and the effects of some operational parameters such as the number of layer and reusability of ZnO nanostructure thin film were examined. The results showed that the five-layer coated glass surfaces have a very high photocatalytic performance.

1. INTRODUCTION

Textile industry wastewater is heavily charged with unconsumed dyes, surfactants, and sometimes traces of metals. These effluents cause a lot of damage to the environment. Many methods, including biosorption [1], conventional activated sludge treatment process [2], electrochemical technologies [3, 4], and reverse osmosis, [5] have been applied on wastewater treatment. However, new environmental laws may consider the spent adsorbents or sludge as hazardous wastes that require further treatment. Consequently, intensive researches on novel technologies with more efficiency and less energy consumption have been stimulated. Photocatalysis using a semiconductor as a photocatalyst is an alternative to conventional methods [6–11]. As a well-known photocatalyst, ZnO has been paid much attention in the degradation and complete mineralization of environmental pollutants. Since ZnO has approximately the same band gap energy (3.2 eV) as TiO_2, its photocatalytic capacity is anticipated to be similar to that of TiO_2. However, the greatest advantage of ZnO is that it absorbs large fraction of the solar spectrum and more light quanta than TiO_2 [12]. Some researches have highlighted the performance of ZnO on degrading some organic compounds [13]. On the other hand, the use of conventional powder catalyst results in disadvantages in stirring during the reaction and in the separation of powder after the reaction. Preparation of film catalysts will make it possible to overcome these disadvantages and to extend the industrial applications [14]. The sol-gel process, as a simple and easy dip-coating means, is one of the versatile methods to prepare thin film-supported nanosized particles without complicated instruments such as CVD. Thin film photocatalysts, with their high photocatalytic ability, high stability, and convenient reuse, have received more and more attention. However, there has been little success in finding thin film photocatalyst that can operate effectively with visible light as yet. In this context, we have paid much attention in preparing thin films of ZnO on glass plates by a sol-gel process and studying its photocatalytic ability for the degradation of X6G an anionic monoazo textile dye. In this paper, a commercial glass-plate was successfully used as substrate to prepare highest *c*-axis oriented ZnO nanostructure thin film by sol-gel dip-coating process. The ZnO/glass films have been employed in photocatalytic degradation of textile dye.

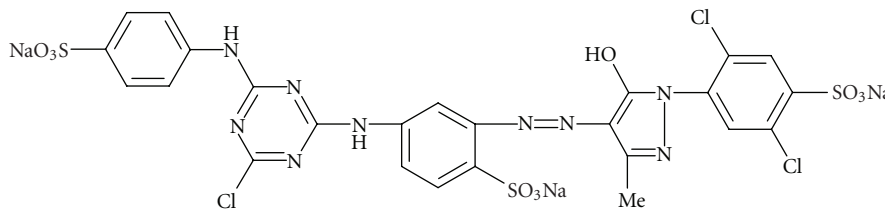

Figure 1: Chemical structure of commercial diazo dye of light yellow (X6G).

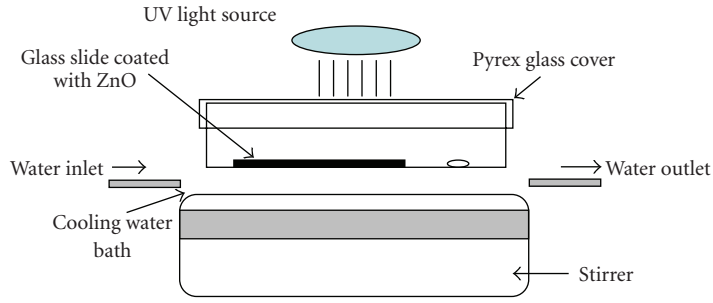

Figure 2: Schematic diagram of photoreactor for degradation.

The result shows that the ZnO/glass film is a photocatalyst with higher activity. It is very interesting and significant to research promising photocatalysts.

2. EXPERIMENTAL

2.1. Preparation of sol

All the chemicals were analytic grade reagents without further purification, and purchased from Merck Company. Light YellowX6G dye (C. I. Reactive Yellow 2, Rmm872.5) was obtained from Youhao (China) and has chemical structure shown in Figure 1. Nanocrystalline ZnO films were prepared on microscope glass slide (75 mm × 25 mm × 1 mm) substrate (washed with ethanol and dilute acid) by a sol-gel method. Sol solution was prepared by adding 3.10 g Zinc acetate dihydrate ($Zn(CH_3COO)_2 \cdot 2H_2O : ZnAc \cdot 2H_2O$), 0.86 g monoethanolamine (MEA), and adequate deionized water to 15 mL isopropanol alcohol, then heated to 60°C with continuous stirring for 60 minutes. The coating substrate (microscope glass slid) was preheated at 275°C for 10 minutes in air after each coating. The sol-gel coating was made usually a day after the sol solution was prepared and the molar ratio of MEA to Zinc acetate was maintained at 1 : 1.

2.2. Film deposition

The films of ZnO were prepared by spin coating method onto substrate with 3000 rpm for 45 seconds(the spinner reached 3000 rpm after 5 s which was maintained for 40 s). Films were annealed at furnace at 550°C for 80 minutes. Precursor solution did not produce any precipitation after 30 days. This spinning-drying procedure was repeated from 2 to 10 times. The microscope glass slide (75 mm × 25 mm ×1 mm: cleaned in dilute HCl solution and ethanol) was used as substrate. Film deposition was carried out in air at room temperature by a rate 3000 rpm for 30 s. After each coating, the films were preheated at 275°C for 10 minutes, and postheated at 550°C for 80 minutes. The deposition was repeated for 2, 4, 5, 6, 8, and 10 times to obtain a film with different thickness.

2.3. Characterization of thin films

The structure and crystalline size were determined by XRD diffraction (Bruker D8 advanced X-ray diffractometer: Cu K_α radiation, Scan rate 0.03 $2\theta\,s^{-1}$). X-ray diffraction shows zincite structure with *c*-axis orientation (002). Optical transmittance was measured by spectrophotometer (Varian Cary 500 Scan).

2.4. Photocatalytic degradation

The photocatalytic degradation experiments were carried out in a simple (40 cm × 15 cm × 15 cm) oxidation reactor (see Figure 2), placed in a 25°C water bath. Slide with 5 layers that placed in 25 mL 10 ppm X6G solution was irradiated with two 8 W lamps (Philips; $\lambda = 365$ nm) placed 5 cm above the solutions. Concentration is measured by spectrophotometer (Varian Cary 500 Scan). In all experiments, 25 mL of 10 ppm X6G solution was used with stirring during the irradiation.

3. RESULTS AND DISCUSSION

3.1. Stability of sol

Sol was prepared by altering the ratio of $Zn(Ac)_2 \cdot 2H_2O$: MEA. In this work, the best sol was obtained with a $Zn(Ac)_2 \cdot 2H_2O$: MEA molar ratio 1 : 1 in isopropanol. Increasing the

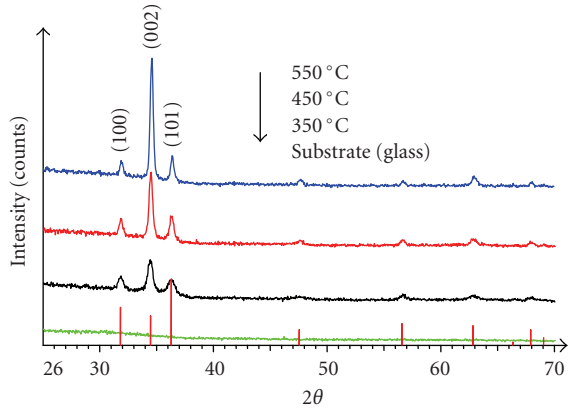

Figure 3: XRD pattern of the ZnO thin films on microscope glass slide by five spin-coatings (5 layers), preheated at 275°C for 10 minutes and postheated for 80 minutes at different temperature.

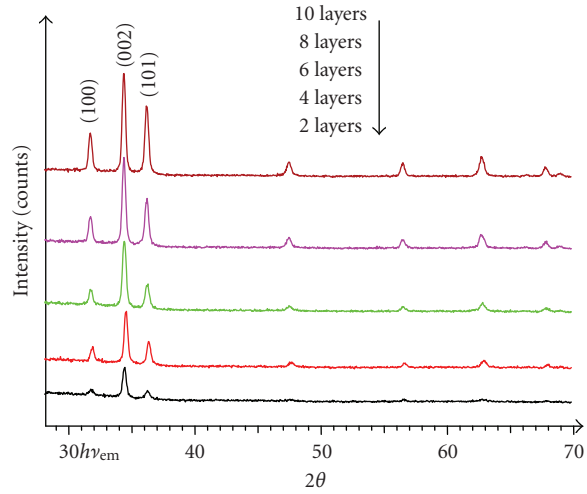

Figure 4: XRD pattern of the ZnO thin films on microscope glass with different layers (2, 4, 6, 8, and 10 layers), preheated at 275°C for 10 minutes and postheated for 80 minutes at 550°C.

water content and decreasing the time of reflux may change the sol to gel immediately. MEA was added to keep the sol solutions stable and clear for a long period (more than 30 days). There are many factors affecting the crystallization behavior of the films such as substrate, the time and temperature of reflux, molar ratio of starting material, and composition of stabilizers such as MEA. In this work, sol was prepared at 60°C for 60 minutes until a clear homogeneous solution appeared. The XRD pattern of the ZnO thin films on microscope glass slide by five spin-coating (5-layer) preheated at 275°C for 10 minutes and postheated for 80 minutes at different temperature, 350°C, 450°C, and 550°C, was shown in Figure 3. There are three distinct differences between the XRD of thin films and ZnO powder. Firstly, diffraction peaks of thin films have lower intensity and higher FWHM (Fully Width at Half Maximum) compared to powder; secondly, the films are predominantly (002) oriented, and finally films are crystallized (wurtzite) at comparatively higher temperature as compared to powder that has been prepared from chemical producers. Increase of annealing temperature affected the intensity of (002) peak which was the highest at 550°C. The ZnO films grow with a (002) orientation is kinetically preferred, which in turn likely reflects the fact that the highest density of Zn atoms is found along the (002) plane [15].

Figure 4 shows the XRD pattern of the ZnO thin film on microscope glass for various layers by spin-coating (2, 4, 6, 8, and 10 layers), preheated at 275°C for 10 minutes and postheated for 80 minutes at 550°C.

Figures 5(a)–5(c) show the scanning electron microscopy (SEM) image of the nanostructure ZnO thin films at various temperatures, and Figure 5(d) shows atomic force microscopy (AFM) image of ZnO thin film at 450°C that prepared by spin coating method on a glass substrate. The average grain size of nanostructure ZnO thin films was near 40 nm, and the crystal size increased with increasing the annealing temperature. As shown in Figures 5(a)–5(d), thin films of ZnO prepared by spin coating reveal the formation of a porous granular surface.

Table 1: The grain size (crystalline size) of ZnO thin films with various times of coating, postheated at 550°C.

Samples of thin film	2θ	FWHM = β	D (nm)
2-layer	34.484	0.350	23.9
4-layer	34.471	0.342	24.7
6-layer	34.743	0.358	23.5
8-layer	34.443	0.335	25.1
10-layer	34.462	0.332	25.1

Optical transmittance of ZnO thin films with 5 times spin coating, preheated at 275°C for 10 minutes and postheated at various temperatures, 350°C, 450°C, and 550°C, is shown in Figure 6. The absorption at about 370 nm corresponds to an electronic transition beyond the bandgap, 3.2 eV of the wurtzite crystalline phase of ZnO.

The crystalline size of ZnO in the films was calculated by Scherrer's formula $D = 0.9\lambda/\beta\text{Cos}\theta$, where D is the grain size, λ (1.548 Å) is the wavelength of X-ray radiation used, β is the full width at half maximum (FWHM) of the diffraction peak, and θ is the Bragg diffraction angle of the XRD peak. The average crystalline size of ZnO in the films annealed at 350°C, 450°C, and 550°C was about 16, 23 and 25 nm, respectively. The average crystalline size of ZnO in the films with various times of coating annealed at 550°C is shown in Table 1. It was observed that the c-axis orientation improves, and the grain size increases as indicated by an increase in intensity of the (002) peak and the decrease in the FWHM (Fully Width at Half Maximum) high with the increase of annealed temperature. An average grain size was about 25 nm.

3.2. Photocatalytic activity

Evaluation of the films as potential photocatalyst for water pollutant purification was based on the degradation of a

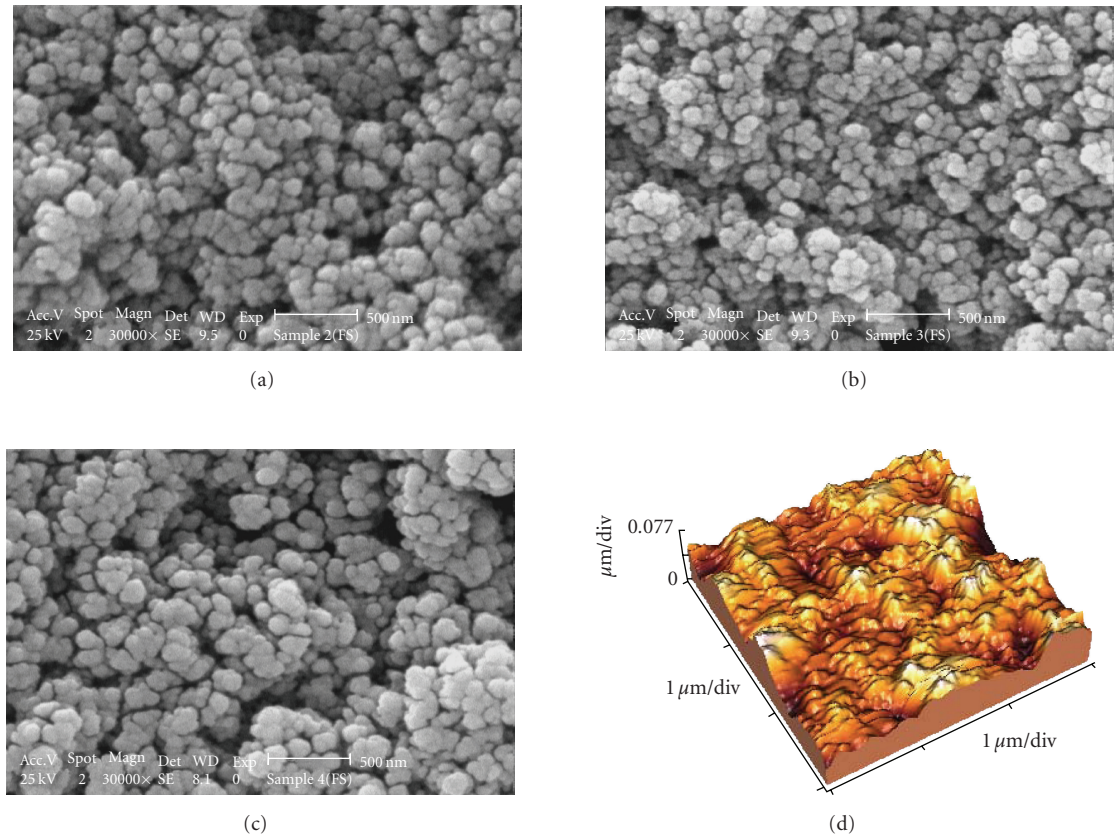

Figure 5: ((a)–(c)) SEM images of the ZnO thin film at different temperature ((a) = 350°C, (b) = 450°C, and (c) = 550°C), (d) AFM image ZnO thin film prepared at 450°C.

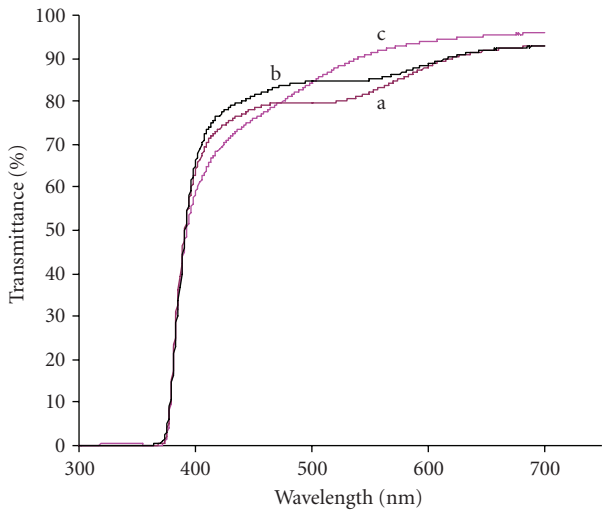

Figure 6: Optical transmittance of ZnO thin films, postheated at various temperatures (a = 350°C, b = 450°C, and c = 550°C).

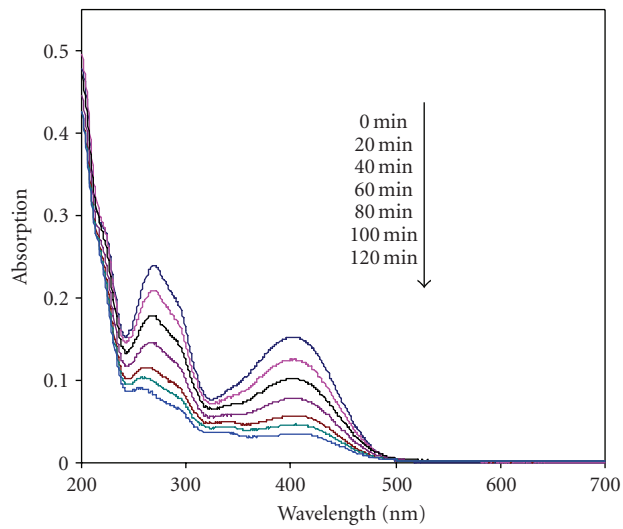

Figure 7: UV-visible spectra of X6G (initial concentration of X6G = 0.013 mM) in deionized water after photocatalytic degradation under UV irradiation on ZnO film with 5 layers.

model azo dye, X6G. The results showed that nanostructure ZnO thin film and UV light (365 nm) had a negligible effect when they were used on their own after 240 minutes. Figure 7 shows the degradation of 10 ppm X6G under UV irradiation (365 nm) using ZnO thin film. Glass plate supported ZnO thin films with different layers (2, 4, 5, 6, 8, and 10 layers)

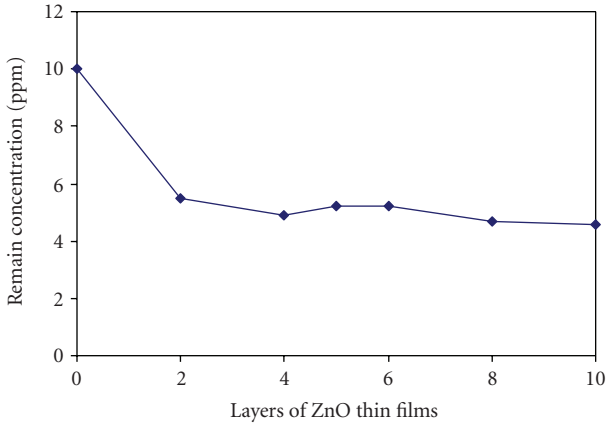

Figure 8: X6G concentration (ppm) (initial concentration of X6G = 0.013 mM) after photocatalytic degradation under UV irradiation for 80 minutes on ZnO films with various layers.

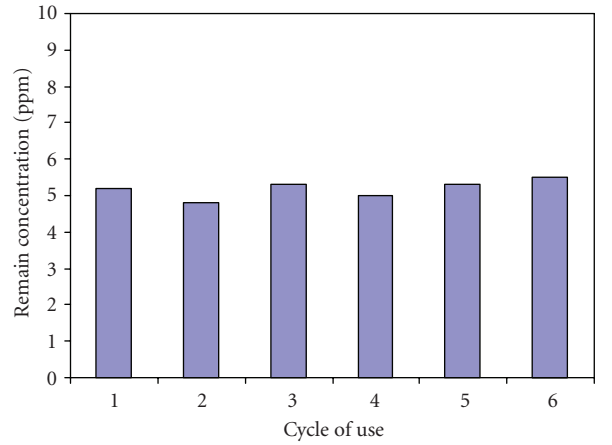

Figure 9: X6G concentration (ppm) (initial concentration of X6G = 0.013 mM) after photocatalytic degradation under UV irradiation for 80 minutes on ZnO film with 5-layer six-cycle reuse.

were tested for degradation of the X6G dye for 80 minutes (see Figure 8).

Thin films with 5 layers were reused five times and did not show much catalytic activity change (see Figure 9).

4. CONCLUSION

Zinc acetate and MEA have proved to be suitable compounds to obtain high quality pure coatings. These precursor compounds and the proper annealing conditions have proved to be suitable to produce stable guest oxide nanocrystalline size. The thin films show good photocatalytic activity for degradation of X6G dye solution.

ACKNOWLEDGMENT

The authors wish to thank the Center of Excellency (Chemistry) University of Isfahan for partial financial support to this work.

REFERENCES

[1] Z. Aksu, "Application of biosorption for the removal of organic pollutants: a review," *Process Biochemistry*, vol. 40, no. 3-4, pp. 997–1026, 2005.

[2] A. Katsoyiannis and C. Samara, "Persistent organic pollutants (POPs) in the conventional activated sludge treatment process: fate and mass balance," *Environmental Research*, vol. 97, no. 3, pp. 245–257, 2005.

[3] G. Chen, "Electrochemical technologies in wastewater treatment," *Separation and Purification Technology*, vol. 38, no. 1, pp. 11–41, 2004.

[4] D. Rajkumar and K. Palanivelu, "Electrochemical treatment of industrial wastewater," *Journal of Hazardous Materials*, vol. 113, no. 1–3, pp. 123–129, 2004.

[5] A. Bódalo-Santoyo, J. L. Gómez-Carrasco, E. Gómez-Gómez, F. Máximo-Martín, and A. M. Hidalgo-Montesinos, "Application of reverse osmosis to reduce pollutants present in industrial wastewater," *Desalination*, vol. 155, no. 2, pp. 101–108, 2003.

[6] A. Fujishima, T. N. Rao, and D. A. Tryk, "Titanium dioxide photocatalysis," *Journal of Photochemistry and Photobiology C*, vol. 1, no. 1, pp. 1–21, 2000.

[7] A Fujishima and K. Honda, "Electrochemical photolysis of water at a semiconductor electrode," *Nature*, vol. 238, pp. 37–38, 1972.

[8] D. Chatterjee and S. Dasgupta, "Visible light induced photocatalytic degradation of organic pollutants," *Journal of Photochemistry and Photobiology C*, vol. 6, no. 2-3, pp. 186–205, 2005.

[9] M. H. Habibi, A. Hassanzadeh, and S. Mahdavi, "The effect of operational parameters on the photocatalytic degradation of three textile azo dyes in aqueous TiO_2 suspensions," *Journal of Photochemistry and Photobiology A*, vol. 172, no. 1, pp. 89–96, 2005.

[10] M. H. Habibi, A. Hassanzadeh, and A. Zeini-Isfahani, "Effect of dye aggregation and azo-hydrazone tautomerism on the photocatalytic degradation of Solophenyl red 3BL azo dye using aqueous TiO_2 suspension," *Dyes and Pigments*, vol. 69, no. 3, pp. 111–117, 2006.

[11] M. H. Habibi and H. Vosoghian, "Photocatalytic degradation of some organic sulfides as environmental pollutants using titanium dioxide suspension," *Journal of Photochemistry and Photobiology A*, vol. 174, no. 1, pp. 45–52, 2005.

[12] S. Sakthivel, B. Neppolian, M. V. Shankar, B. Arabindoo, M. Palanichamy, and V. Murugesan, "Solar photocatalytic degradation of azo dye: comparison of photocatalytic efficiency of ZnO and TiO_2," *Solar Energy Materials and Solar Cells*, vol. 77, no. 1, pp. 65–82, 2003.

[13] C. Lizama, J. Freer, J. Baeza, and H. D. Mansilla, "Optimized photodegradation of reactive blue 19 on TiO_2 and ZnO suspensions," *Catalysis Today*, vol. 76, no. 2–4, pp. 235–246, 2002.

[14] K. Iketani, R.-D. Sun, M. Toki, K. Hirota, and O. Yamaguchi, "Solgel-derived $V_X Ti_{1-X} O_2$ films and their photocatalytic activities under visible light irradiation," *Materials Science and Engineering B*, vol. 108, no. 3, pp. 187–193, 2004.

[15] S. Amirhaghi, V. Cracium, D. Cracium, J. Elders, and I. W. Boyd, "Low temperature growth of highly transparent c-axis oriented ZnO thin films by pulsed laser deposition," *Microelectronic Engineeering*, vol. 25, no. 2–4, pp. 321–326, 1994.

Hindawi Publishing Corporation
Journal of Nanomaterials
Volume 2008, Article ID 384171, 8 pages
doi:10.1155/2008/384171

Research Article

Development of Photocatalytic Active TiO_2 Surfaces by Thermal Spraying of Nanopowders

Filofteia-Laura Toma,[1] Ghislaine Bertrand,[2] Didier Klein,[2] Cathy Meunier,[3] and Sylvie Begin[4]

[1] *Fraunhofer Institute Material and Beam Technology (IWS), Winterbergstrasse 28, 01277 Dresden, Germany*
[2] *Laboratoire d'Etudes et de Recherches sur les Matériaux, les Procédés et les Surfaces (LERMPS), Université de Technologie de Belfort-Montbéliard (UTBM), Site de Sévenans, 90010 Belfort Cedex, France*
[3] *Institut FEMTO-ST (CNRS UMR 6174), 4 Place Tharradin, BP 71427, 25211 Montbéliard, France*
[4] *ECPM-IPCMS-GMI (CNRS UMR 7504), 23 Rue du Loess, BP 43, 67034 Strasbourg, France*

Correspondence should be addressed to Filofteia-Laura Toma, filofteia-laura.toma@iws.fraunhofer.de

Received 4 September 2007; Accepted 13 December 2007

Recommended by Ping Xiao

Titanium dioxide is a very useful photocatalyst for the decomposition and diminution of environmental water and air pollutants. In such applications, it can be used as slurry or as immobilized coating obtained by different deposition methods. The studies performed in the last years showed that thermal spraying could be employed to elaborate TiO_2 coatings with high performance for the decomposition of organic compounds. This manuscript presents a comparative study on the microstructure and photocatalytic performance of titania coatings obtained by different thermal spray techniques: atmospheric plasma spraying (APS), suspension plasma spraying (SPS), and high-velocity oxygen fuel spray process (HVOF). Different titania powders and suspensions were used to study the influence of the feedstock materials on the coating characteristics. The deposits were mainly characterised by SEM and X-ray diffraction. The photocatalytic performance was evaluated from the removal of nitrogen oxides. The experimental results showed that a drastic reduction of the pollutant concentration was obtained in presence of coatings elaborated by suspension plasma spraying. TiO_2 coatings resulting from the spraying of agglomerated powder presentd less efficiency. That was mainly explained by the significant phase transformation from anatase to rutile that occurred in the enthalpic source during the spray processes.

1. INTRODUCTION

Titanium dioxide (TiO_2) is an attractive material for numerous technological processes. It finds applications as gas sensors, as pigments in foodstuffs, paints, cosmetics, or pharmacology, as a corrosion resistant coating, in heterogeneous catalysis and photocatalysis, in solar cells for the production of hydrogen and electric energy, in electronic devices, and so on. After the initial work by Fujishima and Honda [1] on the photolysis of water on TiO_2 electrodes, extensive studies on titania photochemical applications have been carried out in the last few decades. As a photocatalyst, titanium dioxide can be used in the degradation of air and water pollutants, in medical sterilization, and even in cancer therapy [2–4]. Among the two TiO_2 crystalline phases, anatase and rutile that can contribute to the photocatalysis, it is generally assumed that the anatase—the metastable phase, which by thermal treatment irreversibly turns into rutile—allows a higher-photocatalytic degradation of the pollutants. However, some anatase powders containing small quantities of rutile present a better efficiency than those of pure anatase [5, 6]. For the photocatalytic applications, titanium dioxide can be used in powder form (slurry) or immobilized in thin film or coating form obtained by different deposition techniques (sol-gel, dip-coating, and physical or chemical vapour deposition, etc.). TiO_2 powders have an outstanding photocatalytic efficiency compared with their coating counterparts due to their higher specific surface area. However, the separation of powder from the liquid state used in water treatments and recycling processes is troublesome, mainly because of the formation of aggregates. On the other hand, it is considered that the aforementioned difficulties concerning films and coatings can be overcome and their applications can also be expanded by employing various materials as substrates.

Thermal spraying is widely used to prepare titania coatings for mechanical and biomedical applications due to their hardness, wear and corrosion resistance, and biocompatibility [7–12]. The studies performed in the last years showed that the thermal spray technique could be employed to obtain TiO_2 coatings with an effective photocatalytic performance for the decomposition of organic compounds [13–16].

In thermal spraying, the material feedstock (commonly a powder with typical particles size distribution ranging from 10 to 100 μm) is injected in an enthalpic source (thermal plasma or flame obtained by ionization-excitation of inert gases or combustion, resp.). The particles are melted (or partially melted), accelerated by a gas flow, and crushed on the target substrate where rapid solidification and deposit built-up occur. In the last years, a new technique, called liquid thermal spraying, with liquid materials as feedstock precursors was developed [17–24]. The liquid precursors can be (i) organic (ethoxide, butoxide, acetate, etc.) or inorganic (nitrate, chloride, etc.) solutions, and (ii) aqueous or alcoholic suspensions of the material to be sprayed. The suspension allows the feeding of particles with diameters ranging from several nm to 1 μm into the plasma plume. To be used as a precursor in thermal spraying, the slurry (suspension of fine particles in a solvent) has to contain a high-powder load with a low viscosity and a high stability. The deposition depends on different parameters such as the hydrodynamic properties of the liquid which depend on the solid content, droplet diameters, and thermal and kinetics history of the droplets before impinging on the substrate [25].

In this paper, a comparative study on the microstructure and photocatalytic performance of the nanostructured TiO_2 coatings obtained by different thermal spray techniques: atmospheric plasma spraying (APS), suspension plasma spraying (SPS), and high-velocity oxygen fuel (HVOF) spray process is proposed. The coating microstructure was mainly characterized by scanning electron microscopy and X-ray diffraction. The photocatalytic behavior of sprayed coatings was evaluated by a degradation of gaseous nitrogen oxide pollutants (NO, NOx), major air pollutants that cause serious problems on the environment and human health.

2. EXPERIMENTAL PROCEDURE

2.1. Material feedstock

Three commercial TiO_2 powders were used in this study: a pure anatase nanopowder, with 7 nm crystalline size, namely, TiO_2-ST01 (Ishihra Sangyo, Japan) agglomerated by spray-drying in order to prepare spherical microsized anatase particles (with a size distribution ranging from 10 to 50 μm); a 23 nm anatase nanopowder TiO_2-PC105 (Millennium Inorganic Chemicals, France) and TiO_2-P25 powder (Degussa AG, Germany) generally considered as a reference in the photocatalytic applications, containing 80 vol.% anatase (25 nm) and 20 vol.% rutile (50 nm).

Distilled water and ethylic alcohol were used as solvents in the preparation of suspensions, in which the powder load was set to 20–25 wt%. No dispersing agent was added in the composition of the suspensions.

2.2. Thermal spraying

Different thermal spray techniques were used to elaborate nanostructured coatings. Moreover, the spray conditions had been adjusted in order to minimize the particle heat input and to maintain the original anatase phase in the elaborated coating.

Atmospheric plasma spraying (APS) was carried out with a Sulzer-Metco PTF4 plasma gun (6 mm nozzle torch). Ar at 40 $L\cdot min^{-1}$ was used as primary plasma gas; H_2 (3 $L\cdot min^{-1}$) and He (20 $L\cdot min^{-1}$) were added as secondary plasma gases. The arc intensity was about 400 A. Stainless steel substrates ($60\times70\times2$ mm^3) previously sand-blasted were set to 80 and 100 mm from the exit of the nozzle torch. The powder rate was 14 $g\cdot min^{-1}$ and carried by Ar at 3 $L\cdot min^{-1}$.

A special device was designed for the injection of liquid in the plasma [26]. The suspensions were introduced by a peristaltic pump, at a feed rate of about 20–25 $mL\cdot min^{-1}$, in the system that ensured the atomization of the liquid and radial injection of the resulting drops in the plasma jet (Figure 1). Argon at a flow rate of 3–5 $L\cdot min^{-1}$ allowed the atomization of the liquid before entering in the plasma.

High-velocity oxygen flame spraying (HVOF spraying) was performed with a Sulzer-Metco CDS 100 gun (with a 3-inche nozzle) using natural methane, as fuel gas. The flame was obtained by the combustion of 100 $L\cdot min^{-1}$ CH_4 with 400 $L\cdot min^{-1}$ O_2. N_2 at a flow rate of 50 $L\cdot min^{-1}$ was also added to the gas mixture to decrease the flame temperature. The powder feed rate was 20 $g\cdot min^{-1}$ and was carried by N_2 at a flow rate of 9.5 $L\cdot min^{-1}$. The spray distance was set to 150 mm.

2.3. Characterization

The coatings morphology was examined using a JEOL JSM-5800 LV scanning electron microscopy. X-ray diffraction (X'Pert MPD Philips diffractometer) with Cu Kα radiation was used to assess the anatase to rutile ratio. Scan step was 0.02° s^{-1} with a step time of 0.5 second in the 20–90° 2θ range. The volume percentage of anatase was determined according to the relation developed by Berger-Keller et al. [27]. $C_A = 8I_A/(8I_A + 13I_R)$, where I_A and I_R are the X-ray intensities of the anatase (1 0 1) and rutile (1 1 0) peaks, respectively. The crystallite size was evaluated from the X-ray diffraction based on the Scherrer formula.

The photocatalytic performance of TiO_2 was evaluated by the decrease of nitrogen oxides (NO, NOx) concentration in a purpose-built test chamber described elsewhere [28]. A 15-W daylight lamp with a fraction of 30% UVA and 4% UVB ensured the irradiation of the TiO_2. The NO and NOx concentrations were measured continuously using an AC-30M NOx dual chamber analyzer (environmental SA, France) and recorded with a data acquisition system.

The photocatalytic tests were performed over the sprayed coatings and the initial powders. The photocatalytic performances were evaluated as the ratio of the photocatalytic

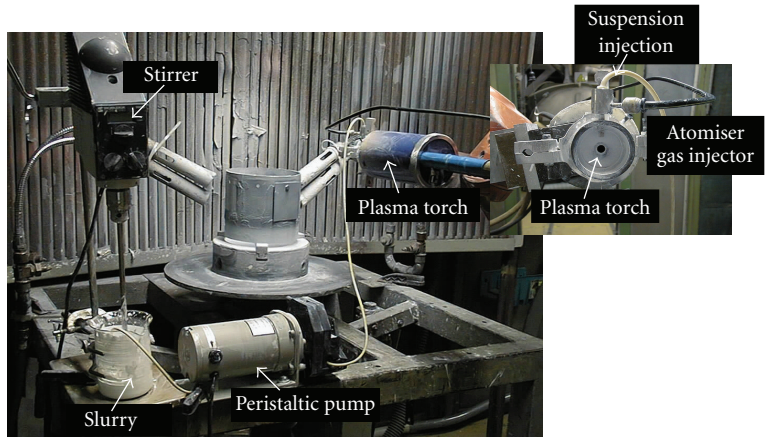

Figure 1: Suspension plasma spraying setup.

conversion of nitrogen oxides and determined by the following relations:

$$\text{NO conversion } (\%) = \frac{[\text{NO}]_{\text{initial}} - [\text{NO}]_{\text{UV}}}{[\text{NO}]_{\text{initial}}} \times 100,$$
$$\text{NOx conversion } (\%) = \frac{[\text{NOx}]_{\text{initial}} - [\text{NOx}]_{\text{UV}}}{[\text{NOx}]_{\text{initial}}} \times 100, \quad (1)$$

where NO conversion (%) and NOx conversion (%) were the photocatalytic removal of NO and NOx concentrations in the presence of the catalyst and UV irradiation; $[\text{NO}]_{\text{initial}}$ and $[\text{NOx}]_{\text{initial}}$ represented the values of the NO and NOx concentrations without UV irradiation; $[\text{NO}]_{\text{UV}}$ and $[\text{NOx}]_{\text{UV}}$ were the values of the NO and NOx concentrations under UV irradiation.

3. RESULTS AND DISCUSSION

3.1. Coating microstructure

3.1.1. Plasma spraying

The morphology of the sprayed coating was mainly dependent on the thermal spray technique. The deposits obtained by the plasma spraying of the agglomerated TiO_2-ST01 nanopowder were characterized by a bimodal microstructure (Figure 2): on the one hand, a thin lamellar morphology commonly observed with sprayed coatings that contained fully melted particles, and on the other hand, a structure of densely agglomerated grains that contained partially melted particles.

When the agglomerated ST01 nanopowder was dispersed in distilled water (25 wt% powder loading) and injected in the plasma jet as a suspension, the microstructure of the resulting coatings did not present the lamellar structure, which is a characteristic of the thermal sprayed coatings. The TiO_2-ST01 suspension-sprayed coatings were relatively porous and constituted of partially melted or unmelted fine particles as depicted in Figure 3. The different microstructure

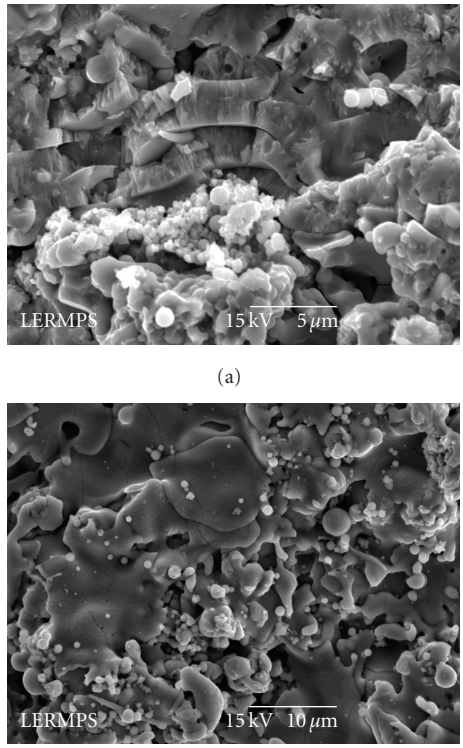

Figure 2: SEM-microstructures of nanostructured TiO_2-ST01 coating prepared by APS technique: (a) fracture; (b) surface.

of the ST01 coatings elaborated by suspension plasma spraying compared with their counterparts obtained from conventional APS was explained by the fact that the thermal transfer between the plasma jet and the material was less important when the suspension was used as feedstock material. In this case, a part of the plasma energy was used to evaporate the solvent of the suspension droplets; the flying time of the resulting particles (free of liquid) was not enough to ensure a complete melting of the particles before impact on substrate.

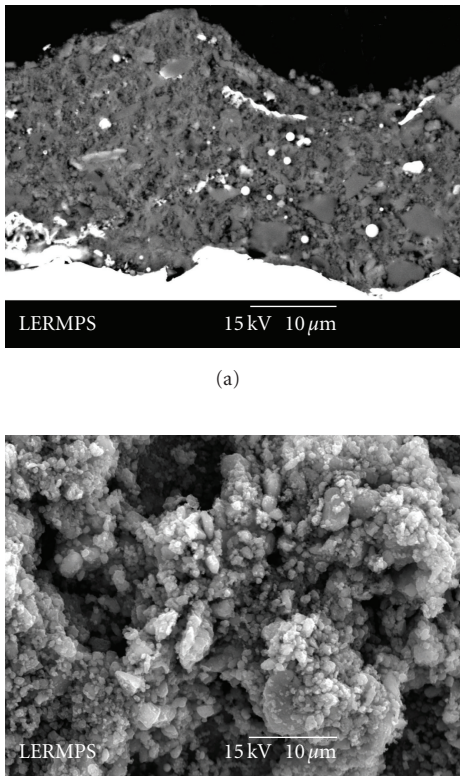

Figure 3: SEM-microstructures of TiO_2-ST01 coating prepared by suspension plasma technique: (a) cross-section; (b) surface.

A nonlamellar microstructure was also observed in the coatings obtained by the plasma spraying of the suspensions (20 wt% powder loading) of nonagglomerated titania powders P25 and PC105. The coatings formed from aqueous suspensions exhibited relatively dense structures (see Figure 4). Moreover, it seemed, at high-microscopic scale, that the coatings were built up by the dense stacking up of fine spherical nanoparticles [29].

Different morphologies were observed in the case of the deposits elaborated from alcoholic suspensions of the two titania nonagglomerated powders. TiO_2-P25 alcoholic suspension-sprayed coating contained melted and nonmelted particles as shown in Figure 5(a). The presence of the melted zones was explained by the fact that the enthalpy of the evaporation of ethanol was lower ($0.8 \cdot 10^6$ J/kg) than that of water ($2.3 \cdot 10^6$ J/kg). Moreover, it was claimed that the injection of an alcoholic suspension in the plasma plume was assumed to increase the jet temperature as well as the gas speed [25]. In this case, the thermal transfer between the plasma and the particles was more important so the particles were easily heated and then melted. Thus, the molten particles had enough momentum to impinge on the substrate and spread out in splat forms like usually achieved in thermal spray process.

The coatings produced from an alcoholic suspension of PC105 particles were porous; different microstructural features were distinguished on the cross-section of the coating: fully melted zones, nonmelted regions, and spherical particles (Figures 5(b), 5(c)). These features were explained by the large distribution of the liquid droplets injected in the plasma as well as the different thermal history of the particles in the enthalpic source before impinging on the substrate. It was interesting to notice the very different microstructures of these coatings compared to that resulting from the P25 alcoholic suspension. This structure was probably due to the different physical properties of the suspensions such as viscosity or surface tension.

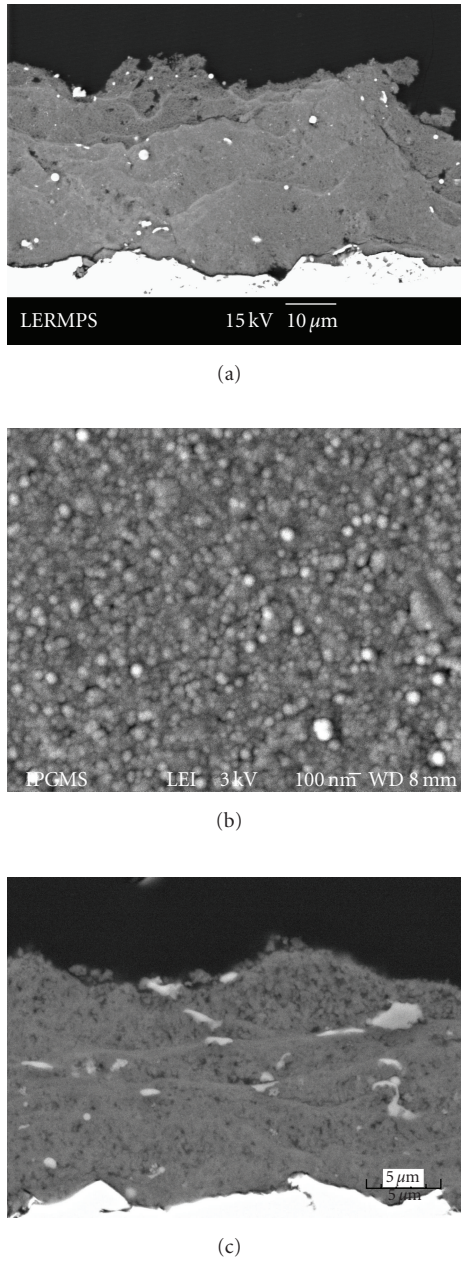

Figure 4: SEM-morphology of coatings starting from aqueous suspensions of (a) TiO_2-P25; (b) TiO_2-P25 at high-microscopic scale; (c) TiO_2-PC105 [29].

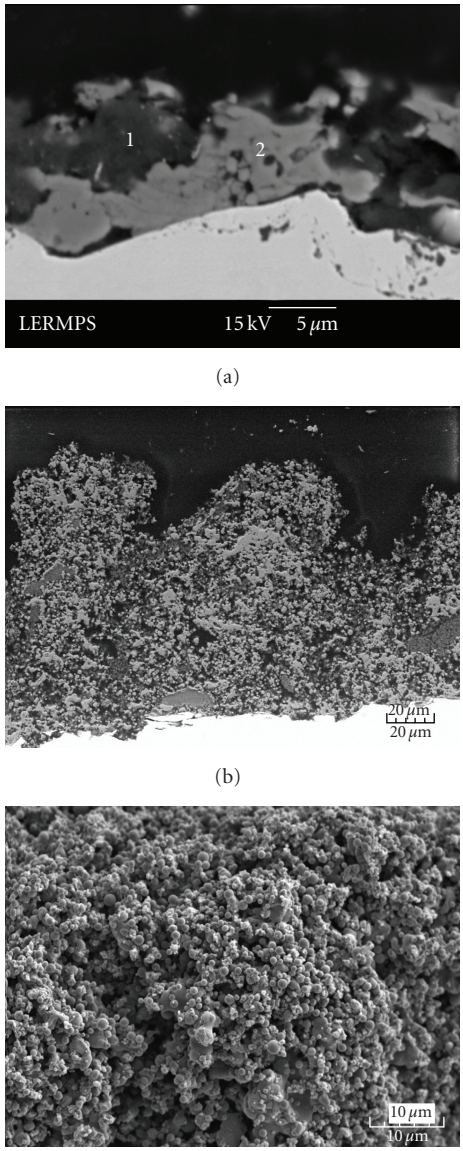

Figure 5: SEM-morphology of coatings starting from alcoholic suspensions of (a) TiO_2-P25, cross-section (1: unmelted regions; 2: melted zones); (b) TiO_2-PC105, cross-section; (c) TiO_2-PC105, surface.

3.1.2. HVOF spraying

The TiO_2 deposits elaborated by the HVOF spraying of agglomerated TiO_2-ST01 nanopowder were porous and characterized by a layered structure (Figure 6). The coatings were mainly built up by the melted nanoparticles impacting on the substrate that flatten to form splats which are consecutively piled on top of the others. Some partially molten particles embedded in the coating structure were also observed. The surface analysis showed the presence of fine particles which conserved the initial features of the agglomerated TiO_2-ST01 nanopowder.

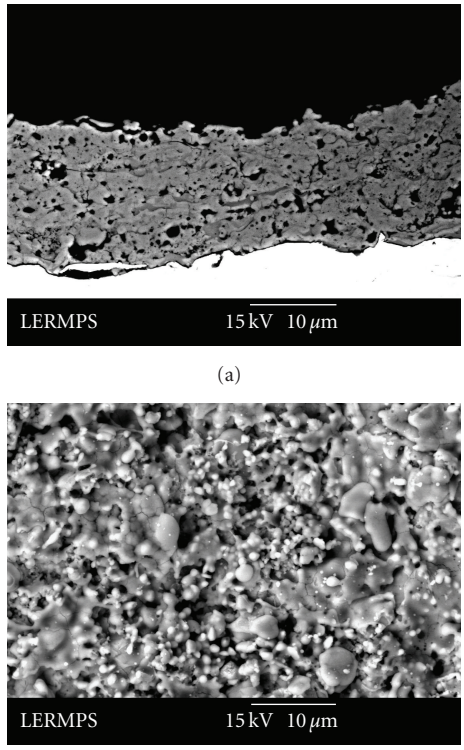

Figure 6: SEM-microstructures of TiO_2-ST01 coating prepared by HVOF technique: (a) cross-section; (b) surface.

3.2. Coating crystalline structure

X-ray diffraction was performed to assess the anatase to rutile ratio. The analysis showed that the passage of the feedstock material (as particles or liquid suspension) in the enthalpic source (plasma or flame) involved the modifications of the chemical state of titanium dioxide compared to that of the initial powders. These structural transformations depended on the thermal spray method used in the elaboration of TiO_2 coatings.

Table 1 resumes the crystalline phases and the crystalline size of the particles determined in different sprayed coatings. The coating elaborated by the plasma spraying of agglomerated ST01 powder contained the rutile structure as a major phase; the anatase content was estimated between 10.9 and 12.2 vol.%. Some traces of TiOx or Magnéli phases were also identified. The crystallite sizes of the anatase increased from 7 nm to 34 nm. An important phase transformation from anatase to rutile was also observed in the coating obtained by HVOF process. In contrast, when the agglomerated ST01 powder was injected in the plasma in form of aqueous suspension, the content of anatase phase was higher than 96 vol.%; furthermore, the crystalline size of anatase was preserved (7.0–7.3 nm), practically identical to that of the original powder.

The crystalline structure of the coating was relative to the melting degree of the particles during spraying. It is generally accepted that the rutile phase corresponds to the fully melted

Table 1: Phases and crystallites size in the thermal sprayed coatings.

Ref. TiO_2 coating	Anatase (vol.%)	Anatase crystallites average size (nm)	Rutile crystallites average size (nm)	Observations (other phases)
ST01-APS	10.9–12.2	19.2–34.8	67.0–78.6	Traces of Magnéli phases (Ti_3O_5; Ti_6O_{11})
ST01-WSC*	>96.0	7.0–7.3	0–25.1	—
ST01-HVOF	12.6	80.0	90.0	—
P25-WSC	77.6–81.4	27.1–29.2	51.7–60.5	—
P25-ASC**	23.0	46.0	120.0	—
PC105-WSC	91.9–95.1	34.9–38.7	140.9–194.9	—
PC105-ASC	36.2	151.1	99.2	—

*WSC-coating resulted from plasma spraying of aqueous suspension.
** ASC-coating resulted from plasma spraying of alcoholic suspension.

particles, whereas the anatase structure was mostly presented in the partially and nonmelted particles [13].

With an aqueous suspension of the agglomerated ST01 nanopowder, the phase transformation was avoided because a part of the plasma energy was used to vaporize the water contained in the liquid droplets. So, the flight time in the plasma jet was not long enough so that the anatase to rutile structural transformation occurred before the particle impact on the substrate.

In the case of suspension spraying of nonagglomerated TiO_2 nanopowders, the XRD analysis showed that the anatase ratio depended on the nature of the solvent (water or alcohol) used in the suspension preparation. The plasma spraying of an aqueous slurry led to coatings where the anatase content and the average crystallite size were almost the same as those identified in the raw powders. On the other hand, the injection of alcoholic suspensions involved the structural transformation from anatase to rutile (about 23 vol.% for P25-coatings and 36 vol.% for PC105 coatings), as well as the increase of the crystallite size of the anatase from 23–25 nm to 150 nm. In this case, the phase transformation was attributed to an easier fragmentation of the alcoholic slurry (due to a lower surface tension of the ethanol), followed by a rapid vaporization of the ethanol. Thus, the flight time of the resulting particles had to be long enough to ensure the partial structural transformation from anatase to rutile.

3.3. *Photocatalytic performance for the degradation of nitrogen oxides*

The photocatalytic properties of the sprayed coatings were evaluated by the diminution of gaseous nitrogen oxides and compared with those obtained in the presence of the corresponding powders. 0.4 g of each powder was uniformly distributed over the entire geometric surface of a Petri dish with 54 cm^2 surface area.

The photocatalytic activities of TiO_2 coatings are represented in Figure 7. Different behaviors in the photocatalytic performances were noticed depending on the spraying parameters and nature of the material feedstock.

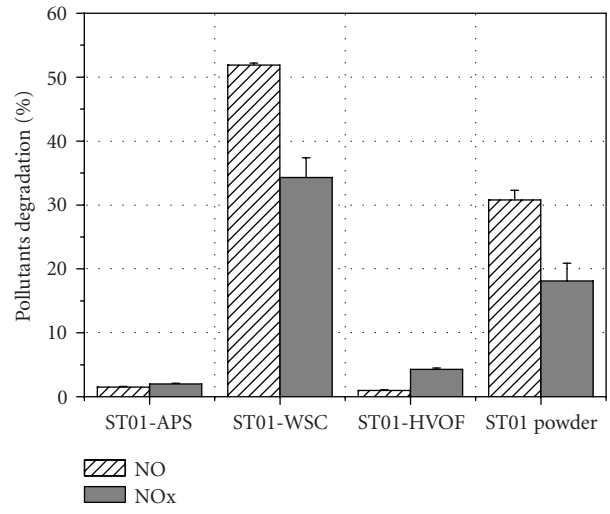

(a)

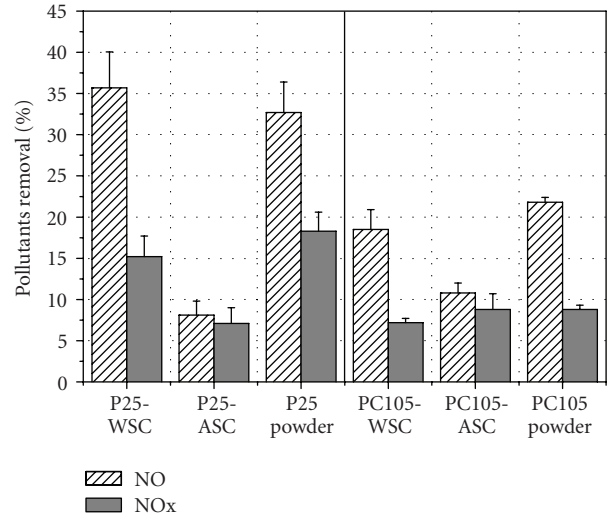

(b)

Figure 7: Photocatalytic degradation of nitrogen oxides in presence of coatings elaborated from (a) agglomerated ST01 nanopowder; (b) nonagglomerated P25 and PC105 nanopowders.

A very low degradation of nitrogen oxide pollutants (<5%) was obtained in presence of the TiO_2 surfaces produced by APS and HVOF sprayings of agglomerated ST01 nanopowder. Other authors reported good photocatalytic responses of APS- or HVOF-sprayed TiO_2 coatings in the decomposition of different organic compounds such as phenol, acetaldehyde, or methylene blue [13–16]. Moreover, the photocatalytic properties of sprayed coatings were improved by the doping of TiO_2 with Pt [30], metallic oxides such as Al_2O_3, Fe_3O_4, ZnO, SnO_2 [31–33], or hydroxyapatite [34]. In our case, the lower-photocatalytic efficiency of APS- and HVOF-sprayed coatings was also correlated with the chemistry and reactivity of nitrogen oxides that are more complex than that of other molecules [35].

When the ST01 powder was injected in aqueous suspension form, the sprayed coating ensured a substantial removal of the nitrogen oxides (around 52% for NO and 34% for NOx), much higher than that of the powder (31% for NO and 18% for NOx). High rates of degradation of gaseous pollutants were also recorded in the presence of aqueous suspension plasma sprayed coatings of nonagglomerated nanopowders P25 (around 36% for NO and 15% for NOx) and PC105 (around 18% for NO and 8% for NOx), comparable with that measured in the presence of the powders. Meanwhile, a lower degradation of pollutants (8–10%) was obtained for the coating resulting from the plasma spraying of alcoholic suspensions.

The different photocatalytic performances were principally correlated with the crystalline structures of the sprayed coating. Anatase phase was a key parameter in the photocatalytic activity and a higher-anatase ratio with reduced crystallite size allowed a better degradation of nitrogen oxides. Besides, the titania deposits elaborated by the spraying of aqueous ST01 and P25 suspensions provided a higher performance than that of the raw powders. In these cases, the enhanced photocatalytic performance could not be explained considering only the anatase ratio. It was assumed that the removal of the impurities coming from the raw powder elaboration and a cleaning up of the free-water particles when crossing the plasma could explain such behavior. Different techniques of surface investigations (infrared spectroscopy and X-ray photoelectrons spectroscopy) performed on the surface of P25 aqueous suspension sprayed coating [29] showed the presence of a higher hydroxylation compared to that on the raw powder surface. The hydroxyl groups played a beneficial role and enhanced the photocatalytic activity of titania as already reported in the literature [36, 37].

4. CONCLUSION

This paper proposed a comparative study on the microstructure and photocatalytic properties of titanium dioxide coatings obtained by different thermal spray methods: atmospheric plasma spraying, suspension plasma spraying, and high-velocity oxygen fuel process using agglomerated and nonagglomerated TiO_2 nanopowders as feedstock materials. The coatings elaborated by APS and HVOF techniques were characterized by the common lamellar microstructure observed in all thermal sprayed deposits. Besides, the use of agglomerated nanoparticles as feedstock materials involved an important phase transformation from anatase to rutile. The photocatalytic ability for nitrogen oxides was lower than 5% and was correlated principally with the reduced anatase content.

The coatings elaborated by suspension plasma spraying presented a specific structure that depended on the nature of the solvent used in the preparation of the suspensions. The anatase crystalline structure and the crystallite size were preserved in the coatings resulting from an aqueous suspension, whereas a significant phase transformation occurred with alcoholic suspensions. Furthermore, the aqueous suspension sprayed coatings presented a remarkable photocatalytic efficiency that in some conditions was higher than that of the corresponding powder.

It can be concluded that the suspension plasma spraying is an appropriate technique to elaborate active titania surfaces for the photocatalytic reduction of reactive gaseous pollutants such as nitrogen oxides.

ACKNOWLEDGMENT

F.-L. Toma wishes to thank Alexander von Humboldt Foundation (Bonn, Germany) for the research fellowship at Fraunhofer Institute-IWS (Dresden, Germany).

REFERENCES

[1] A. Fujishima and K. Honda, "Electrochemical photolysis of water at semiconductor electrode," *Nature*, vol. 238, no. 5358, pp. 37–38, 1972.

[2] D. F. Ollis and H. Al-Ekabi, *Photocatalytic Purification and Treatment of Water and Air, Proceedings of the 1st International Conference*, Elsevier, New York, NY, USA, 1993.

[3] A. Mills and S. Le Hunte, "An overview of semiconductor photocatalysis," *Journal of Photochemistry and Photobiology A*, vol. 108, no. 1, pp. 1–35, 1997.

[4] A. Fujishima, T. N. Rao, and D. A. Tryk, "Titanium dioxide photocatalysis," *Journal of Photochemistry and Photobiology C*, vol. 1, no. 1, pp. 1–21, 2000.

[5] D. C. Hurum, A. G. Agrios, K. A. Gray, T. Rajh, and M. C. Thurnauer, "Explaining the enhanced photocatalytic activity of Degussa P25 mixed-phase TiO_2 using EPR," *Journal of Physical Chemistry B*, vol. 107, no. 19, pp. 4545–4549, 2003.

[6] T. Ohno, K. Tokieda, S. Higashida, and M. Matsumura, "Synergism between rutile and anatase TiO_2 particles in photocatalytic oxidation of naphthalene," *Applied Catalysis A*, vol. 244, no. 2, pp. 383–391, 2003.

[7] W. W. Dai, C. X. Ding, J. F. Li, Y. F. Zhang, and P. Y. Zhang, "Wear mechanism of plasma-sprayed TiO_2 coating against stainless steel," *Wear*, vol. 196, no. 1-2, pp. 238–242, 1996.

[8] R. Gadow and D. Scherer, "Composite coatings with dry lubrication ability on light metal substrates," *Surface and Coatings Technology*, vol. 151-152, pp. 471–477, 2002.

[9] S. O. Chwa, D. Klein, F.-L. Toma, G. Bertrand, H. Liao, C. Coddet, and A. Ohmori, "Microstructure and mechanical properties of plasma sprayed nanostructured TiO_2-Al composite coatings," *Surface and Coatings Technology*, vol. 194, no. 2-3, pp. 215–224, 2005.

[10] A. Ibrahim, R. S. Lima, C. C. Berndt, and B. R. Marple, "Fatigue and mechanical properties of nanostructured and conventional titania (TiO_2) thermal spray coatings," *Surface*

and Coatings Technology, vol. 201, no. 16-17, pp. 7589–7596, 2007.

[11] H. Li, K. A. Khor, and P. Cheang, "Titanium dioxide reinforced hydroxyapatite coatings deposited by high velocity oxy-fuel (HVOF) spray," *Biomaterials*, vol. 23, no. 1, pp. 85–91, 2002.

[12] R. S. Lima and B. R. Marple, "Thermal spray coatings engineered from nanostructured ceramic agglomerated powders for structural, thermal barrier and biomedical applications: a review," *Journal of Thermal Spray Technology*, vol. 16, no. 1, pp. 40–63, 2007.

[13] C. Lee, H. Choi, C. Lee, and H. Kim, "Photocatalytic properties of nano-structured TiO_2 plasma sprayed coating," *Surface and Coatings Technology*, vol. 173, no. 2-3, pp. 192–200, 2003.

[14] A. Ohmori, H. Shoyama, S. Matsusaka, K. Ohashi, K. Moriya, K. Moriya, and C.-J. Li, "Study of photo-catalystic character of plasma sprayed TiO_2 coatings, thermal spray: surface engineering via applied research," in *Proceedings of the 1st International Thermal Spray Conference*, C. C. Berndt, Ed., pp. 319–323, ASM International, Montréal, Québec, Canada, 2000.

[15] E.-A. Lee, S.-W. Lee, C.-H. Choi, H.-S. Kim, and B. Hockey, "Effect of TiO_2 powder size on the reactivity of photocatalyst," *Materials Science Forum*, vol. 439, pp. 288–296, 2003.

[16] G.-J. Yang, C.-J. Li, F. Han, and A. Ohmori, "Microstructure and photocatalytic performance of high velocity oxy-fuel sprayed TiO_2 coatings," *Thin Solid Films*, vol. 466, no. 1-2, pp. 81–85, 2004.

[17] G. Schiller, M. Müller, and F. Gitzhofer, "Suspension plasma spraying for the preparation of perovskite powders and coatings," in *Thermal Spray: A United Forum for Scientific and Technological Advances*, C. C. Berndt, Ed., pp. 349–352, ASM International, Materials Park, Ohio, USA, 1997.

[18] P. Blazdell and S. Kuroda, "Plasma spraying of submicron ceramic suspensions using a continuous ink jet printer," *Surface and Coatings Technology*, vol. 123, no. 2-3, pp. 239–246, 2000.

[19] K. Wittmann, F. Blein, J. Fazilleau, J.-F. Coudert, and P. Fauchais, "A new process to deposit thin coatings by injecting nanoparticles suspensions in a DC plasma jet," in *Proceedings of the International Thermal Spray Conference (ITSC '02)*, E. Lugscheider, Ed., pp. 519–522, DVS Düsseldorf, Essen, Germany, March 2002.

[20] M. Gell, L. Xie, X. Ma, E. H. Jordan, and N. P. Padture, "Highly durable thermal barrier coatings made by the solution precursor plasma spray process," *Surface and Coatings Technology*, vol. 177-178, pp. 97–102, 2004.

[21] R. Tomaszek, Z. Znamirowski, L. Pawlowski, and A. Wojnakowski, "Temperature behaviour of titania field emitters realized by suspension plasma spraying," *Surface and Coatings Technology*, vol. 201, no. 5, pp. 2099–2102, 2006.

[22] A. Killinger, M. Kuhn, and R. Gadow, "High-velocity suspension flame spraying (HVSFS), a new approach for spraying nanoparticles with hypersonic speed," *Surface and Coatings Technology*, vol. 201, no. 5, pp. 1922–1929, 2006.

[23] J. Oberste-Berghaus, J.-G Legoux, C. Moreau, F. Tarasi, and T. Chráska, "Mechanical and thermal transport properties of suspension thermal sprayed alumina-zirconia composite coatings," in *Proceedings of the International Thermal Spray Conference and Exposition, Global Coating Solutions (ITSC '07)*, B. R. Marple, M. M. Hyland, Y.-C. Lau, C.-J. Li, R. S. Lima, and G. Montavon, Eds., pp. 627–632, ASM International, Beijing, China, May 2007.

[24] P. Fauchais, R. Etchart-Salas, C. Delbos, et al., "Suspension and solution plasma spraying of finely structured layers: potential application to SOFCs," *Journal of Physics D*, vol. 40, no. 8, pp. 2394–2406, 2007.

[25] J. E. Döring, R. Vaßen, and D. Stöver, "Influence of carrier gas flow and liquid injection in the plasma jet on plasma characteristics during the atmospheric plasma spray process," in *Proceedings of the International Thermal Spray Conference and Exposition, Advancing the Science & Applying the Technology (ITSC '03)*, C. Moreau and B. Marple, Eds., pp. 641–647, ASM International, Orlando, Fla, USA, May 2003.

[26] F.-L. Toma, G. Bertrand, S. O. Chwa, C. Meunier, D. Klein, and C. Coddet, "Comparative study on the photocatalytic decomposition of nitrogen oxides using TiO_2 coatings prepared by conventional plasma spraying and suspension plasma spraying," *Surface and Coatings Technology*, vol. 200, no. 20-21, pp. 5855–5862, 2006.

[27] N. Berger-Keller, G. Bertrand, C. Filiatre, C. Meunier, and C. Coddet, "Microstructure of plasma-sprayed titania coatings deposited from spray-dried powder," *Surface and Coatings Technology*, vol. 168, no. 2-3, pp. 281–290, 2003.

[28] F.-L. Toma, S. Guessasma, D. Klein, G. Montavon, G. Bertrand, and C. Coddet, "Neural computation to predict TiO_2 photocatalytic efficiency for nitrogen oxides removal," *Journal of Photochemistry and Photobiology A*, vol. 165, no. 1–3, pp. 91–96, 2004.

[29] F.-L. Toma, G. Bertrand, S. Begin, C. Meunier, O. Barres, D. Klein, and C. Coddet, "Microstructure and environmental functionalities of TiO_2-supported photocatalysts obtained by suspension plasma spraying," *Applied Catalysis B*, vol. 68, no. 1-2, pp. 74–84, 2006.

[30] Y. Zeng, W. Wu, S. Lee, and J. Gao, "Photocatalytic performance of plasma sprayed Pt-modified TiO_2 coatings under visible light irradiation," *Catalysis Communications*, vol. 8, no. 6, pp. 906–912, 2007.

[31] A. Ohmori, F.-X. Ye, and C.-J Li, "The effects of the additives on photocatalytic performance of plasma sprayed titanium dioxide coatings," in *Proceedings of the International Thermal Spray Conference, (ITSC '02)*, E. Lugscheider, Ed., pp. 165–169, DVS Düsseldorf, Essen, Germany, March 2002.

[32] Y. Zeng, J. Liu, W. Wu, and C. Ding, "Photocatalytic performance of plasma sprayed TiO_2-$ZnFe_2O_4$ coatings," *Surface and Coatings Technology*, vol. 200, no. 7, pp. 2398–2402, 2005.

[33] H. Chen, S. W. Lee, T. H. Kim, and B. Y. Hur, "Photocatalytic decomposition of benzene with plasma sprayed TiO_2-based coatings on foamed aluminum," *Journal of the European Ceramic Society*, vol. 26, no. 12, pp. 2231–2239, 2006.

[34] F.-X Ye, A. Ohmori, T. Tsumura, K. Nakata, and C.-J. Li, "Microstructures and compositions of photocatalytic plasma-sprayed titania-hydroxyapatite coatings," in *Proceedings of the International Thermal Spray Conference and Exposition, Global Coating Solutions (ITSC '07)*, B. R. Marple, M. M. Hyland, Y.-C. Lau, C.-J. Li, R. S. Lima, and G. Montavon, Eds., pp. 341–346, ASM International, Beijing, China, May 2007.

[35] G. Brasseur, *Physique et chimie de l'atmosphère moyenne*, Masson, Paris, France, 1982.

[36] J. S. Dalton, P. A. Janes, N. G. Jones, J. A. Nicholson, K. R. Hallam, and G. C. Allen, "Photocatalytic oxidation of NO_x gases using TiO_2: a surface spectroscopic approach," *Environmental Pollution*, vol. 120, no. 2, pp. 415–422, 2002.

[37] S. Devahasdin, C. Fan Jr., K. Li, and D. H. Chen, "TiO_2 photocatalytic oxidation of nitric oxide: transient behavior and reaction kinetics," *Journal of Photochemistry and Photobiology A*, vol. 156, no. 1-3, pp. 161–170, 2003.

Hindawi Publishing Corporation
Journal of Nanomaterials
Volume 2008, Article ID 712985, 4 pages
doi:10.1155/2008/712985

Research Article

Field Effect on Crystal Phase of Silicon in $Si/CeO_2/SiO_2$ Structure

Dmitry E. Milovzorov

Fluens Technology Group, Scientific Institute of Physical and Chemical Researches Moscow, Vorontsovo pole 10, Shelkovskoe Shosse 871225, 107497 Moscow, Russia

Correspondence should be addressed to Dmitry E. Milovzorov, dmilovzorov2002@yahoo.com

Received 6 September 2007; Revised 20 January 2008; Accepted 16 March 2008

Recommended by Robert Dorey

The structural, optical, and conductivity properties of silicon film deposited on cerium dioxide buffer layer were studied. The electronic structure of system consists of various defect levels inside band gap. The temperature spatial distribution plays a great role in silicon crystallization. The field destruction of crystal phase and its restoration, after annealing, were investigated.

1. INTRODUCTION

In recent years, thin silicon films deposited on glass are widely used in various fields of electronic industry such as thin film transistors [1], integration circuits, photodetectors, and light-emitting devices. The main problem to improve parameters of electronic devices is the preparation of the crystalline homogenious thin film. However, the thin film (with thickness around 100 nm) deposition on glass substrate does not open possibility to check surely its properties, from one side, and to get crystalline material, from another side. In some instances, an amorphous film is deposited, and after annealing its crystallinity is improved. The other way is to deposit a buffer layer to prevent randomization in bonding by the deposition of silicon thin film on silicon oxide substrate. Cerium dioxide is a suitable dielectric (E_{bg} = 5.5 eV) with a crystal lattice parameter similar to silicon crystal structure to design the ultra-large-scale integration devices. Its dielectric constant is higher than 25, because by thin film transistors, making the leakage current for cerium dioxide thin dielectric layer with thickness of 2.8 nm is four orders of magnitude lower than ordinary SiO_2 dielectric layer [2] at an applied bias of 2 V.

In our work, we studied the field-stimulated destruction of crystal phase in silicon thin film deposited on ultrathin layer of cerium dioxide, and the recrystalization by annealing. The results of this research work can be applied to memory devices design and creation of silicon cluster structures inside amorphous phase, including silicon nanowires. It is seen that only the silicon bonding as crystal structure can be made easily by preparing the preliminary temperature field of substrate. In this case, we can easily obtain the fine crystal structures on glass substrate with significant density of packaging for integration circuit. In addition, such crystal structure can be easily destroyed and restored because of memory effect.

Due to the possibility of large area deposition of thin silicon film on glass, we can achieve the large amount of elements in one unit. The magnetron sputtering of cerium dioxide combined with plasma-enhanced chemical vapor deposition (PECVD) technique results in potential industrial application of product.

2. EXPERIMENTS

2.1. Film preparation

Thin silicon film was deposited by using PECVD method. The gas mixture of silane and hydrogen was used. The temperature of deposition was in the range of 480–570 K. The buffer layer of cerium oxide was deposited on glass directly by using magnetron sputtering system. Its thickness was varied from 1 to 10 nm. Figure 1 shows the Raman spectrum of silicon film deposited on CeO_2 buffer layer. The

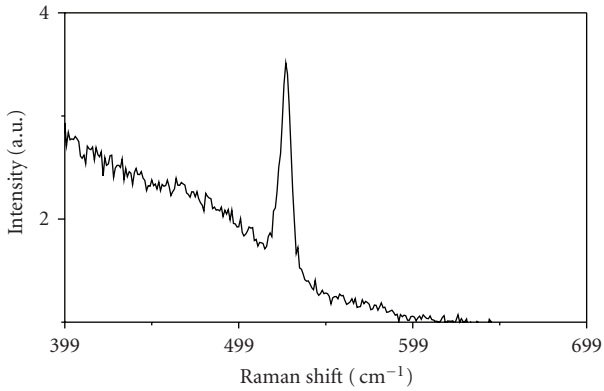

Figure 1: Raman spectrum of silicon film deposited on cerium oxide buffer layer with thickness of 1 nm.

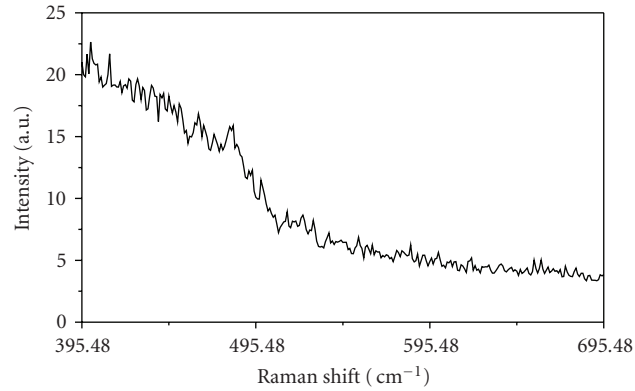

Figure 3: Raman spectrum of silicon film by electric field applying. There is only amorphous phase, and no crystal. Crystal silicon bonding was destructed.

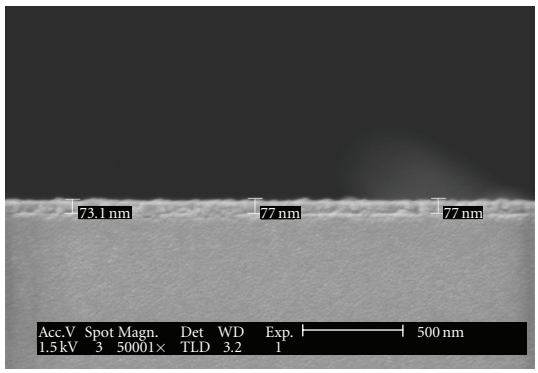

Figure 2: Scanning electron microscope data of silicon film (thickness being around 80 nm) deposited on cerium oxide layer and glass substrate (Corning 1737).

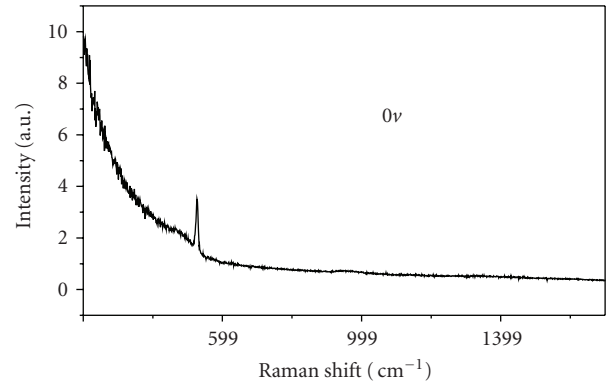

Figure 4: Raman spectrum of silicon film after 30-minute annealing at a temperature of 473 K.

measurements were done by means of probe Ar laser beam with wavelength of 488 nm, and were detected by double monochromator (Jobin Ivon, Kyoto, Japan) coupled with photo multiplier tube.

3. FIELD EFFECT ON SILICON FILM

3.1. Raman spectra

Figure 2 shows the scanning electron microscopic photo of silicon film deposited on glass substrate with buffer CeO_2 thin layer. Also, we studied the Raman spectra (Figure 3) by applying the electrical field 3–6 μV/A. It is seen that the crystal phase-related peak with position around 520 cm^{-1} has disappeared.

By annealing the sample with silicon film deposited on cerium dioxide layer, we obtained Raman data on the appearance of crystalline-related spectral peak around 520 cm^{-1} (see Figure 4), which were measured without application of external electric field. Silicon film was annealed in 30 minutes at a temperature of 473 K. The Raman scattering at elevated temperatures can be explained by quantum Raman susceptibility [3].

3.2. Conductivity measurements

Conductivity measurements as a function of annealing temperature are shown in Figure 5. The silicon film deposited on Corning 7059 substrate has activation energy of 0.2 eV and high value of conductivity due to the high concentration of defects and high crystallinity. The lower conductivity corresponds to the silicon film deposited on thin buffer layer of cerium dioxide because of low content of crystal phase ($E_{bg} = 1.12$ eV) and high fraction of amorphous phase with energy band gap of $E_{bg} = 1.77$ eV.

3.3. Local factors on micro- and nanoscales

The equations for local factors determination on nanoscopic and microscopic scales are strictly different. For microscopic scale, the dipole local field factors surrounding is significant as for nonlinear [4] as well as linear optical response:

$$L(\omega,\rho) = \frac{\rho}{4\pi}\frac{(\varepsilon_c(\omega)-\varepsilon_a(\omega))}{1+(\varepsilon_c(\omega)-\varepsilon_a(\omega))(\Lambda-\beta\rho)}, \quad (1)$$

where ε_c and ε_a are dielectric functions of crystalline and amorphous silicon, respectively. For sphere depolarization

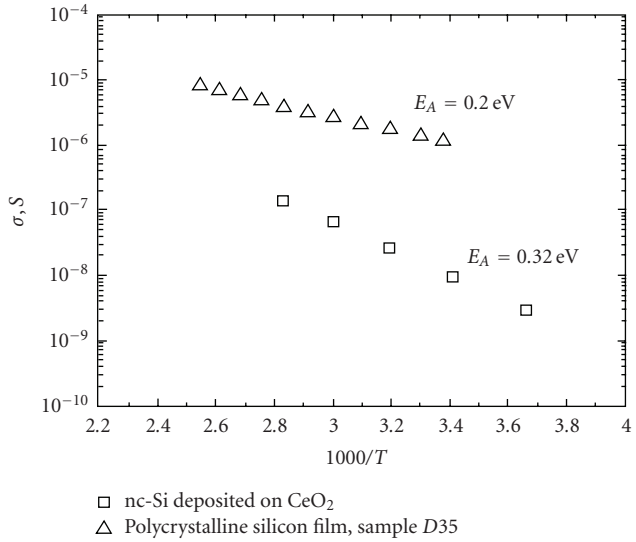

Figure 5: Conductivity measurements of silicon films deposited on glass substrates, Corning 7059 and Corning 1737, with cerium oxide buffer layer of 1 nm.

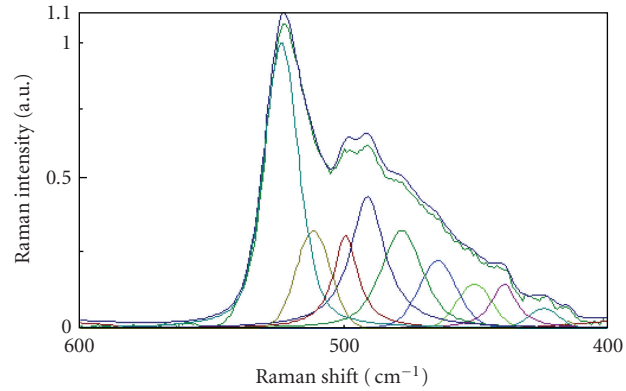

Figure 6: Raman spectrum deconvoluted by using Gauss and Lorentz peaks. The Ce–O bonding is a related 456–460 cm^{-1} spectral peak.

factor Λ is equal to 1/3, β is the Lorentz constant ($\beta = 1/3$ for a homogeneous spherical surrounding).

The crystal phase homogeneity on the microscope is low, compared to silicon films with large thickness. The crystallization of silicon here mainly depends on the crystallization of cerium dioxide layer. Figure 6 shows the Raman spectrum for silicon film deposited on cerium dioxide buffer layer by high-temperature (600°C) conditions. It is seen that the crystal phase-related spectral peak around 520 cm^{-1} and wide spectra peak extended from 440 cm^{-1} to 500 cm^{-1}. The spectral deconvolution illustrates eight main oscillators with defined eigenfrequencies. One of them with position 456 cm^{-1} is related to the Ce–O dipoles. Silicon nanocrystal bonds that are weaker than bulk crystal bonding cause the spectral peak around 500 cm^{-1}.

For nanoscopic scale, the local field factor (see Figure 8) is determined by tensor of polarizability [5]. Dielectric susceptibility tensor can be written as

$$\chi_{\alpha\beta} = \partial P_\alpha / \partial E_\beta, \tag{2}$$

where P_α is the component of polarization along the Cartesian coordinates, and E_β is the component of external field. The film polarization mainly contributed to various components of dipole moments along the coordinates, particularly the dipoles Si–O–Si on film surface and intergrains boundary. We can estimate the value of dipole moment by the angle between the two Si–O bonds being around 90° using formula for quantum dipole:

$$\mu^{\text{Si–O–Si}}_{2p\text{O}-3p\text{Si}} = 2\sqrt{2}\pi e \int_0^{\xi}\int_0^{2\pi}\int_0^{\pi} \Psi_{3p_x\text{Si}}\Psi_{3p_y\text{Si}} r \Psi_{2p_x-\text{O}}\Psi_{2p_y-\text{O}} r^2 dr d\varphi d\theta. \tag{3}$$

The dipole moment is equal to the 1.4 D. The orientation of dipoles inside silicon film plays a great role in optical response because of strong asymmetrical properties and sufficient polarization charge. It is necessary to note that the electron wave function in Si–O–Si configuration is distributed among the 12 silicon atoms [6], because, to calculate the tensor value for $Si/CeO_2/SiO_2$ structure for thin silicon film, we can use the linear combination of all components along the coordinates:

$$\chi_{\text{Silicon-film}}{}^{(1)} = \chi^{(1)}{}_{\text{Si–O Intergrain}} + \chi_{\text{film-surface}}{}^{(1)} + \chi^{(1)}{}_{\text{CeO–Si Interface}}. \tag{4}$$

Figure 7 shows the microscopic homogeneity of crystal phase for silicon film. The crystal phase is inhomogeneously laterally distributed according to surface temperature fields' variations. Figure 8 illustrates the morphology of silicon film surface. It is clear that using dipole-surrounding calculations can combine the local factor field. The Si–O bonding on silicon film surface plays a great role in local factor value determination. For more detailed description to calculate local factor field value, we use the silicon nanocrystal orientation, oxygen atoms incorporation on silicon surface, as well.

4. MODEL OF FIELD DESTRUCTION

4.1. Silicon clusters and nanowires

The structural properties of silicon film deposited on crystalline buffer layer of cerium dioxide strictly depend on the cerium dioxide crystallinity lateral distribution. The cerium dioxide nanocrystals are deposited by magnetron target sputtering at determined temperature of substrate. Increasing the temperature of substrate causes the increase in cerium dioxide nanocrystal lateral density, because, by using the definite silicon film preparation, the appearance of silicon crystal nanostructures with single bonding is observed. Such single-bonding one-dimensional structure can extend through the silicon film. Silicon nanoclusters and nanowires made by applying nanoscopic temperature field consist of

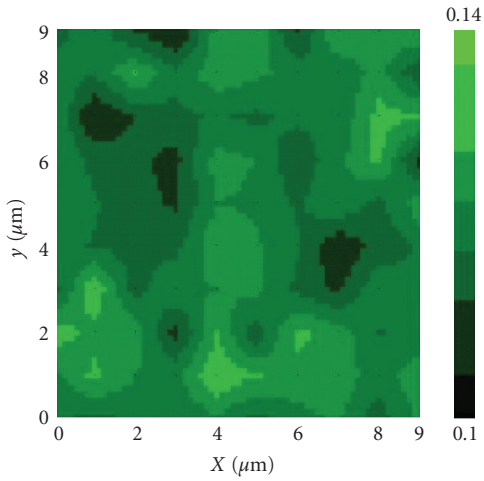

Figure 7: Raman mapping measurements of silicon crystal phase for silicon film deposited on CeO_2 buffer layer. Thickness of buffer layer is 90 nm.

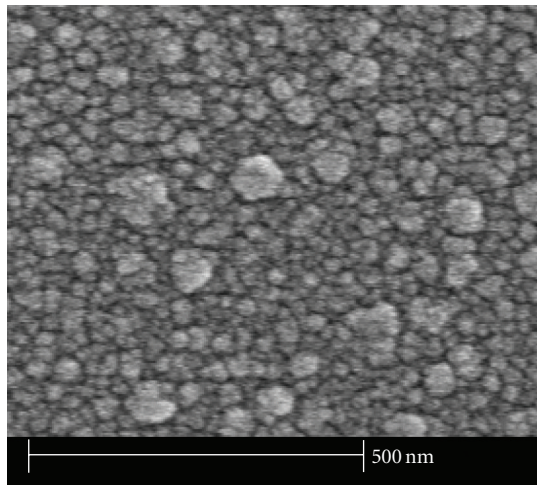

Figure 8: The microscopic photo of silicon film.

silicon bonding with surely one-dimension scale. The field-stimulated destruction can only be achieved by silicon-silicon bond elimination and defect creation such as dangling bond. The memory effect for nanostructured silicon crystals can be observed by annealing the $Si/CeO_2/SiO_2$ structure. It is clear that the appearance of crystal phase every time by annealing depends on the minimums of potential energy that are determined by cerium dioxide nanocrystals' spatial positions.

4.2. Oxygen incorporated into Silicon

For thin silicon films (thickness being less than 100 nm) deposited on silicon oxide, the concentration of oxygen atoms is significant. Usually, the oxygen atoms are incorporated with silicon in grain boundary of nanocrystals by complicated surface morphology of film, because the proposed model [7] of stabilized silicon-oxygen incorporation in the grain boundary after transformation of the silanol groups into strong siloxane bonds was calculated for two types of structures: 13 silicon atoms incorporated with 14 atoms of oxygen (SiO_x, $x \approx 1$) by the Si–O bond angle being equal to 130°, the size of glass cluster is around 8.86 Å; 29 silicon atoms incorporated with 39 oxygen atoms ($x \approx 1.34$) create the glass cluster size being equal to 14.77 Å. The consequence of the saddle points in potential energy of oxygen atom was changed by the stress [8].

4.3. Role of cerium dioxide

For the silicon crystallization in thin silicon film, the role of crystallized clusters of cerium dioxide is great. The crystallization conditions of cerium oxide layer are different from the silicon film deposition conditions. Because of the high temperature of cerium silicide creation, we suppose that the main role in silicon crystallization is played by a temperature field on substrate.

ACKNOWLEDGMENTS

The author thanks the Associate Professors A. Kazansky and Paul Forsh from Moscow State University for their assistance in conductivity measurements. Also, he acknowledges Mr. Ramesh Kakkad for cerium oxide preparation, and thanks Professors Shimizu and S. Hasegawa from Kanazawa University, who helped him in the PECVD preparation of silicon films.

REFERENCES

[1] D. P. Gosain, "Low temperature poly-Si TFT for mobile display applications," in *Proceedings of the 9th Asian Symposium on Information Display (ASID '06)*, pp. 32–37, New Delhi, India, October 2006.

[2] T. M. Pan, C. H. Chien, T. F. Lei, T. S. Chao, and T. Y. Huang, "Electrical characteristics of thin cerium oxide film on silicon substrate by reactive DC sputtering," *Electrochemical and Solid-State Letters*, vol. 4, no. 9, pp. F15–F17, 2001.

[3] A. Compaan and H. J. Trodahl, "Resonance Raman scattering in Si at elevated temperatures," *Physical Review B*, vol. 29, no. 2, pp. 793–801, 1984.

[4] D. E. Milovzorov and T. Suzuki, "Size-dependent second-harmonic generation by nanocrystals prepared by plasma-enhanced chemical-vapor deposition," *Applied Physics Letters*, vol. 75, no. 26, pp. 4103–4105, 1999.

[5] D. E. Milovzorov, "Quantum properties of thin silicon films and silicon/ silicon dioxide interfaces," in preparation.

[6] G. D. Watkins and J. W. Corbett, "Defects in irradiated silicon. I. Electron spin resonance of the Si-A center," *Physical Review*, vol. 121, no. 4, pp. 1001–1014, 1961.

[7] D. E. Milovzorov, "Polycrystalline silicon for semiconductor devices," in *Micro- and Nanoelectronics*, vol. 5401 of *Proceedings of SPIE*, pp. 208–218, Zvenigorod, Russia, October 2004.

[8] L. Dobaczewski, O. Andersen, L. Rubaldo, et al., "Saddle point for oxygen reorientation in the vicinity of a silicon vacancy," *Physical Review B*, vol. 67, no. 19, Article ID 195204, 8 pages, 2003.

Hindawi Publishing Corporation
Journal of Nanomaterials
Volume 2008, Article ID 475168, 5 pages
doi:10.1155/2008/475168

Research Article

Metallic Nanoparticles Embedded in a Dielectric Matrix: Growth Mechanisms and Percolation

M. García del Muro,[1] Z. Konstantinovic,[1] M. Varela,[2] X. Batlle,[1] and A. Labarta[1]

[1] *Departament de Física Fonamental i Institut de Nanociència i Nanotecnologia, Universitat de Barcelona, Martí i Franquès 1, 08028 Barcelona, Spain*
[2] *Departament de Física Aplicada i Òptica i Institut de Nanociència i Nanotecnologia, Universitat de Barcelona, Martí i Franquès 1, 08028 Barcelona, Spain*

Correspondence should be addressed to M. García del Muro, montse@ffn.ub.es

Received 1 October 2007; Accepted 26 December 2007

Recommended by Ping Xiao

We present a study of the preparation and structural characterization of granular Ag-ZrO_2, Co-ZrO_2, and Au-ZrO_2 thin films grown by pulsed laser deposition (PLD) in a wide range of volume fraction x of metal ($0.08 < x_{Ag} < 0.28$, $0.06 < x_{Co} < 0.40$, and $0.08 < x_{Au} < 0.55$). High-resolution transmission electron microscopy (HRTEM) showed regular distribution of spherical Au, Co, and Au nanoparticles having very sharp interfaces with the amorphous matrix. The structural results are compared aiming to stress the effect of the actual microstructure on the percolation threshold. Two different mechanisms of particle growing as a function of the metal content are evidenced: nucleation and particle coalescence, with their relative significance depending strongly on the type of metal, giving rise to very different values of the percolation threshold (x_c(Ag)~0.28, x_c(Co)~0.35, and x_c(Au)~0.55).

1. INTRODUCTION

The latest great advances in fine particle systems field have been promoted by the development of new measuring techniques and refinement of synthesis methods allowing the preparation of particles at the nanometric scale with promising technological applications in many different fields. In particular, granular films, in which a distribution of ultrafine metallic particles is embedded in a dielectrix matrix, comprise a very active research topic. From a fundamental point of view, these composite systems show a variety of behaviors related to percolation processes that the standard percolation theories have not satisfactorily explained yet [1–3]. From technological aspect, spherical particles of noble metals homogeneously dispersed in dielectric matrix exhibit promising optical applications [4–6], associated with its large third-order nonlinear susceptibility [7–9] and ultrafast response [10] when approaching percolation. When the metal is magnetic, granular magnetic solids are excellent materials to study basic properties, such as finite-size interaction and surface effects, and enhanced and tailored properties [11]. From the technological point of view, their magnetic and magnetotransport properties also suggest attractive applications, including high coercive films for information storage [12, 13], high-permeability high-resistivity films for shielding and bit writing at high frequencies [14], and giant magnetoresistance for read heads and magnetic sensors [15].

In this paper, we present the preparation and structural characterization by HRTEM of granular Ag-ZrO_2, Co-ZrO_2, and Au-ZrO_2 thin films grown by PLD from a single composite target within a wide range of volume fraction x of metal, from the dielectric regime until percolation ($0.08 < x_{Ag} < 0.28$, $0.06 < x_{Co} < 0.40$, and $0.08 < x_{Au} < 0.55$). Statistical analysis of TEM images provides us with the mean size and width of the size distribution as a function of metal concentration. In particular, we observe that for the three prepared metals, the mean size of the particles increases in a very different way with the metal content. The role played by the two identified growing mechanisms (coalescence and nucleation) is shown to be very different in these three systems, and so leading to different percolation threshold.

2. EXPERIMENTAL

Ag-ZrO_2, Co-ZrO_2, and Au-ZrO_2 granular films were grown by KrF laser ablation (wavelength of 248 nm, pulse duration

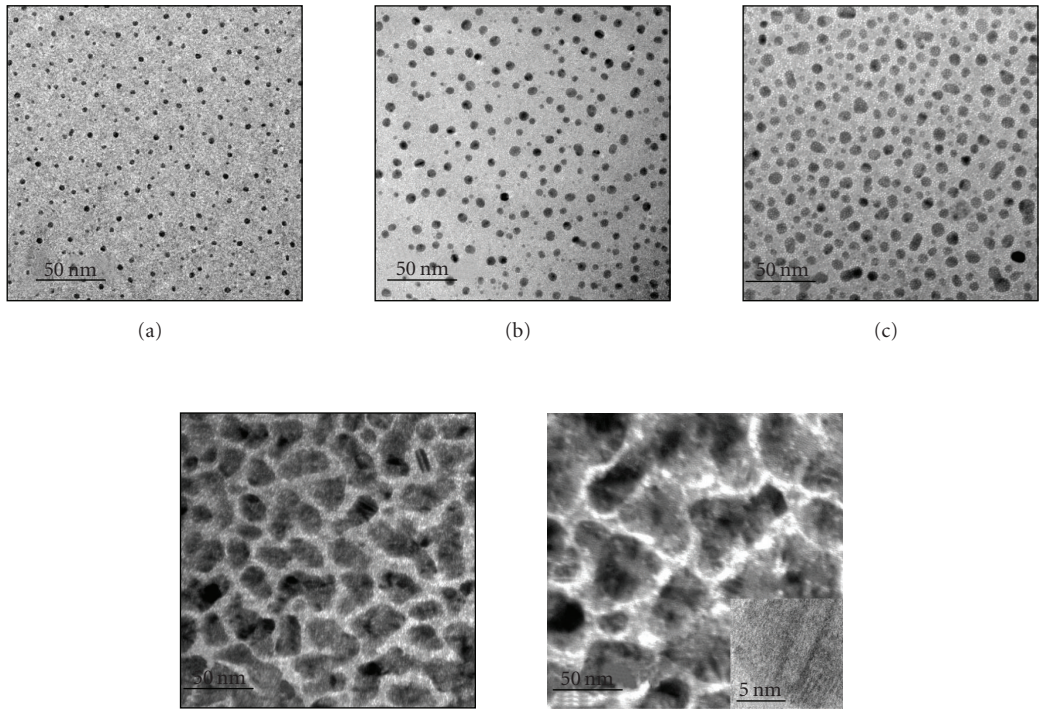

Figure 1: Bright field TEM images of Ag-ZrO_2 films with (a) $x = 0.08$, (b) $x = 0.18$, (c) $x = 0.23$, (d) $x = 0.26$, and (e) $x = 0.28$. The scale length is indicated in each image. The inset in Figure 1(e) shows lattice fringes inside an Ag particle.

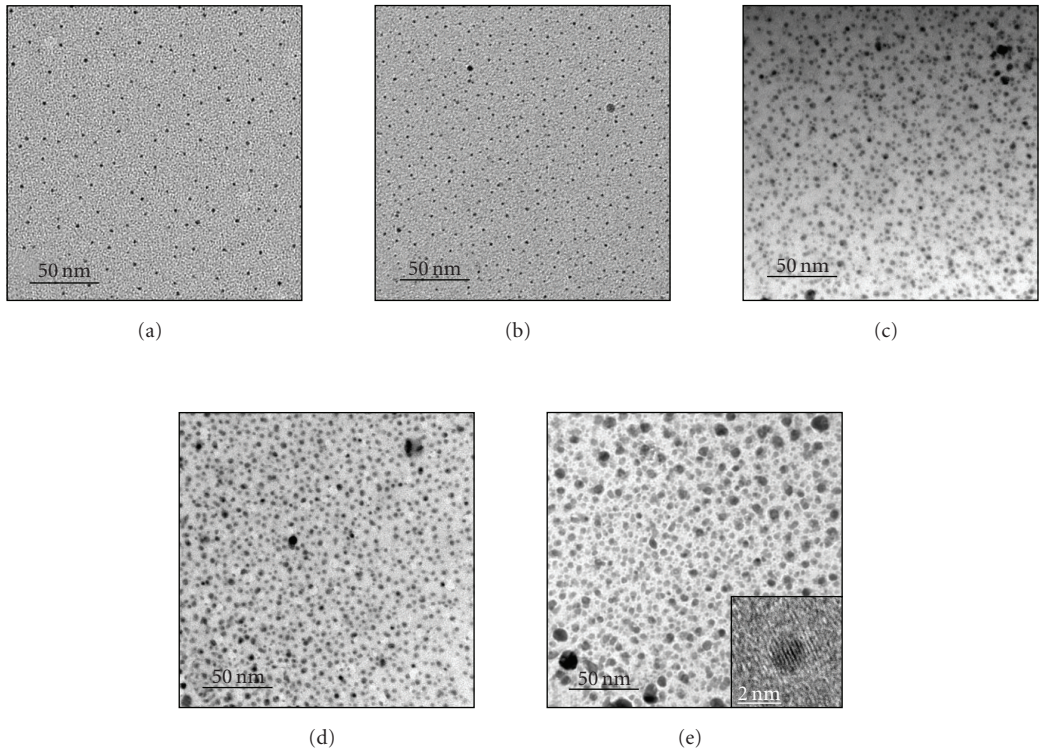

Figure 2: Bright field TEM images of Co-ZrO_2 films with (a) $x = 0.06$, (b) $x = 0.12$, (c) $x = 0.25$, (d) $x = 0.30$, and (e) $x = 0.35$. The inset in Figure 2(e) shows lattice fringes inside a Co particle.

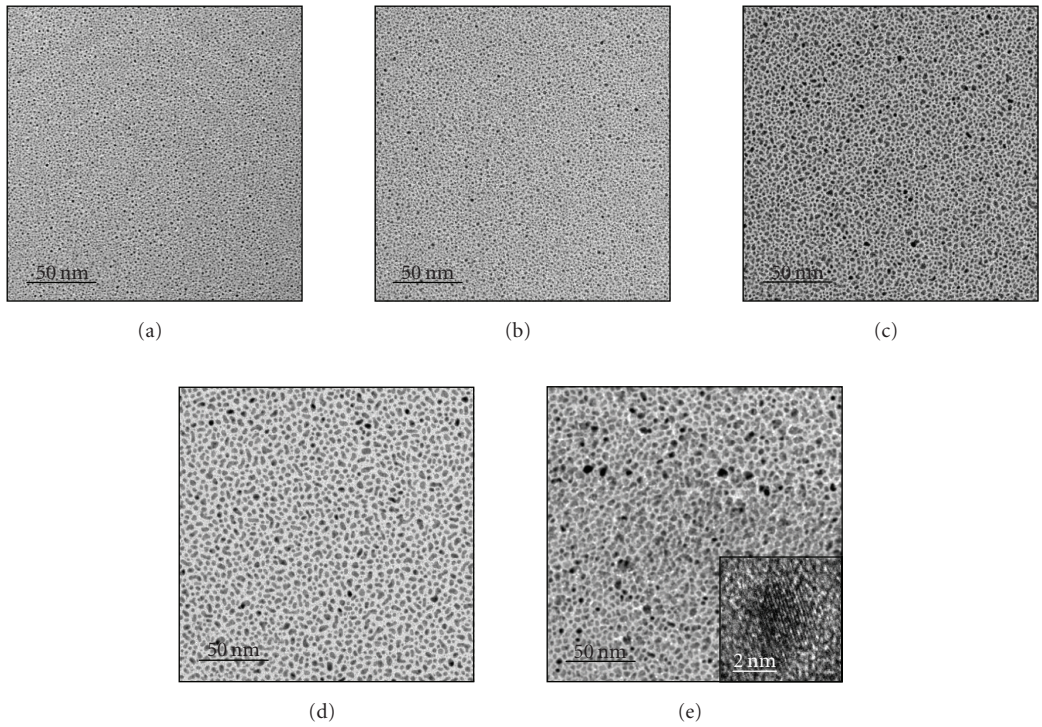

FIGURE 3: Bright field TEM images of Au-ZrO_2 films with (a) $x = 0.08$, (b) $x = 0.23$, (c) $x = 0.41$, (d) $x = 0.51$, and (e) $x = 0.55$. The inset in Figure 3(e) shows lattice fringes inside an Au particle.

of $\tau = 34$ ns). The samples were deposited at room temperature in a vacuum chamber with rotating composite targets made of sectors of ZrO_2 and metal (silver, cobalt, or gold). Several surface ratios of target components led to obtainning samples with different volume fractions x of Ag/Co/Au, ranging from metallic to dielectric regimes. The distance between target and substrate was fixed to 35 mm. The laser fluency typically used was about 2 J/cm^2. Zirconia was stabilized with 7 mol.% Y_2O_3, which provides the matrix with very good properties, such as good oxidation resistance, thermal expansion coefficient matching that of metal alloys, and very high fracture toughness values. It has been observed that ZrO_2 matrix gives rise to sharper interfaces between the amorphous matrix and nanoparticles [16]. Besides, the high oxygen affinity of ZrO_2 prevents oxidation of the metallic nanoparticles.

Sample composition was determined by microprobe analyses. The size distribution of metal nanoparticles was determined from TEM. The substrates for TEM experiments were membrane windows of silicon nitride, which enabled direct observation of as-deposited samples.

3. RESULTS AND DISCUSION

The analysis of TEM images allowed us to obtain the particles size distribution for each metal concentration. TEM images provide direct observation of the nanoparticles even for very low metal contents. Typical TEM images are shown in Figure 1 for Ag-ZrO_2, in Figure 2 for Co-ZrO_2, and in Figure 3 for Au-ZrO_2. The dark regions correspond to the Ag, Co, and Au particles and the light regions to the amorphous ZrO_2 matrix. The particles are seen to have clearly defined interfaces with the matrix.

The lattice fringes observed in the metal grains correspond to Ag/Co/Au atomic planes indicating good crystallinity even for very low metal content (see insets to Figures 1–3). Lattice fringes are not present in the ZrO_2 matrix, confirming its amorphous nature.

The particles have spherical shape for $x_{Ag} < 0.18$, $x_{Co} < 0.25$, and $x_{Au} < 0.41$, (see Figures 1(a) and 1(b), 2(a)–2(c), and 3(a) and 3(b)). For $x_{Ag} > 0.18$, $x_{Co} > 0.25$, and $x_{Au} > 0.41$, the neighboring particles start to coalesce, giving rise to larger particles not always with spherical shape (see elongated particles in Figures 1(b)–1(d), 2(d), and 3(c) and 3(d)). Increasing the metal content, the particles form big aggregates (see Figures 1(e), 2(e), and 3(e)), indicating rapid approaching to the percolation threshold, above which metal forms a continuum.

The distributions of particle size are well described by a log-normal function:

$$f(D) = \frac{1}{\sqrt{2\pi}\sigma D} \exp\left[- \frac{\ln^2(D/D_0)}{2\sigma^2} \right], \qquad (1)$$

where the fitting parameters D_0 and σ are the most probable particle size and the width of the distribution, respectively, (see Table 1). At low Ag content, the particle size distribution is centered between 1 and 2 nm (see Figure 1(a)). Increasing the Ag content, the size distribution shifts towards larger sizes, due to coalescence of smaller particles into the big ones,

Table 1: Particle size distribution parameters obtained from TEM data as a function of the metal volume concentration (x): D_0 (most probable diameter), D_M (average particle diameter, $D_M = D_0 \exp(\sigma^2/2)$), and σ (with of the distribution).

x_{Ag}	D_0 (nm)	D_M	σ
0.08	1.7	1.8	0.40
0.18	11	11.2	0.20
0.23	17	17.4	0.22
0.26	39	39.9	0.21
0.28	220	249.3	0.50
x_{Co}	D_0 (nm)	D_M	σ
0.06	2.0	2.0	0.20
0.12	2.7	2.8	0.25
0.25	7	7.4	0.35
0.30	10.5	11.0	0.30
0.35	14	15.5	0.45
x_{Au}	D_0 (nm)	D_M	σ
0.08	1.2	1.3	0.45
0.23	2	2.2	0.40
0.41	3	3.3	0.45
0.51	5.9	6.1	0.25
0.55	9.5	10	0.32

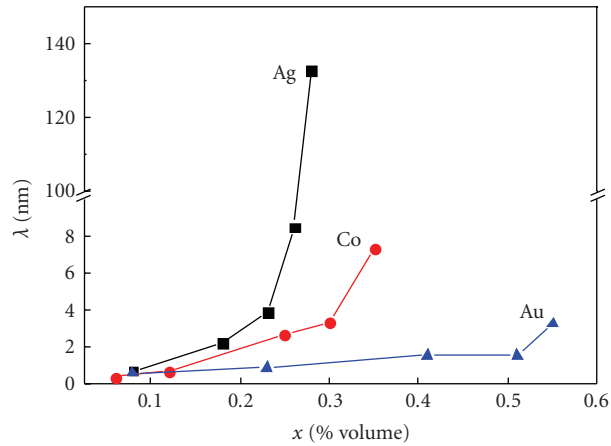

Figure 4: Standard deviation of the size distribution versus metal content.

which produces a net narrowing effect on the particle size distribution (σ goes from 0.4 to 0.2). About $x_{Ag} = 0.28$, the size distribution broadens abruptly ($\sigma = 0.5$) because of massive coalescence of the nanoparticles taking place at percolation.

A quite different evolution of the microstructure is observed for Au-ZrO_2 as the Au content is increased. At low Au content, the width of the particle size distribution is similar to that observed for silver with $x_{Ag} = 0.08$. Nevertheless, in this case, a very smooth shift of the size distribution towards larger sizes is observed even for Au contents as high as $x_{Au} = 0.41$ (see Table 1), suggesting that in a wide range of concentrations Au particles tend to be coated by the matrix, which minimizes particle coalescence and maintains the width of the size distribution almost constant. The onset of coalescence processes takes place about $x_{Au} > 0.41$, giving rise to a similar narrowing of the size distribution (from $\sigma = 0.45$ to $\sigma = 0.25$) as it is also observed in Ag-ZrO_2, but in this case occurring at metal contents very close to percolation. Finally, at $x_{Au} \sim 0.55$ massive coalescence of the nanoparticles arising from percolative processes takes place, which produces a broadening of the size distribution, as it is also observed for Ag-ZrO_2. In the case of the Co-ZrO_2 system, the evolution of the microstructure is closer to Au than to Ag. The coalescence is observed to start about $x_{Co} > 0.25$ (see Figure 2(d)), where the width of the size distribution becomes narrower (see Table 1), and a final increase in σ is observed for $x_{Co} = 0.35$, anouncing percolation.

Average particle size for silver, cobalt, and gold increases with metal concentration, but following very different behaviors. With increasing Au content, mean particle size slightly increases, since in this case and below about $x_{Au} = 0.04$, particles grow essentially by condensation of the gold atoms available in the neighborhood of each nucleating seed, according to TEM images (see Figures 3(a) and 3(b)). However, for Ag-ZrO_2, the mean particle size increases abruptly with x_{Ag} because particle growth is arising from nucleation and further coalescence of neighboring particles even at low metal contents. The Co-ZrO_2 is an intermediate case between the extreme behaviors of Au-ZrO_2 and Ag-ZrO_2.

The role played by the two different mechanisms of particle growing observed in Ag-ZrO_2, Co-ZrO_2, and Au-ZrO_2 granular films gives rise to very different values of the percolation threshold in these granular materials. The approach to percolation with the metal content can be better evidenced by the abrupt increase of the standard deviation of the size distribution, defined as $\lambda = D_M[\exp(\sigma^2) - 1]^{1/2}$ [17]. Figure 4 shows the variation of $\lambda(x)$. The metal contents, at which massive particle coalescence preceding percolation takes place, correspond to the range of the $\lambda(x)$ curves where a significant departure from linear behavior is observed. For Ag-ZrO_2, percolation threshold deduced from Figure 4 and according to TEM images ($x_c(Ag) \sim 0.28$) is very close to the theoretical prediction for the model of random percolation of hard spheres [18]. In contrast, particle coalescence in Co-ZrO_2 and Au-ZrO_2 is inhibited by the better efficiency of the matrix to coat the particles with respect to silver ones, which retards the occurrence of percolating processes, shifting the critical value of the metal content to $x_c(Co) \sim 0.35$ and $x_c(Au) \sim 0.55$.

4. CONCLUSIONS

We have shown that pulsed laser deposition is an appropriate technique to prepare silver, cobalt, and gold nanoparticles embedded in ZrO_2 matrix, in a wide range of volume concentration ($0.08 < x_{Ag} < 0.28$, $0.06 < x_{Co} < 0.40$, and $0.08 < x_{Au} < 0.55$). Sharp interfaces between rounded crystalline particles and amorphous matrix are observed in the as-prepared samples, without needing ulterior thermal treatment. The mean nanoparticle diameter increases with metal

volume concentration, but through different mechanisms depending on the metal element. Silver nanoparticles are obtained in a wider range of diameters (1–200 nm) than that corresponding to cobalt (2–15 nm) and gold ones (1–10 nm) which were observed obtained under the same preparation conditions. Distinct microstructures are shown to be the consequence of the relative contribution of the two particle-growing mechanisms: nucleation and particle coalescence. Consequently, the percolation thresholds are very different in these three systems, ($x_c(\mathrm{Ag}) \sim 0.28$, $x_c(\mathrm{Co}) \sim 0.35$, and $x_c(\mathrm{Au}) \sim 0.55$).

ACKNOWLEDGMENTS

The authors would like to thank the staff of the scientific and technical facilities of the University of Barcelona. Financial support of the Spanish CICYT (MAT2006-03999) and Catalan DURSI (2005SGR00969) is recognized.

REFERENCES

[1] F. Brouers, J. P. Clerc, G. Giraud, J. M. Laugier, and Z. A. Randriamantany, "Dielectric and optical properties close to the percolation threshold. II," *Physical Review B*, vol. 47, no. 2, pp. 666–673, 1993.

[2] A. B. Pakhomov, X. Yan, and B. Zhao, "Giant Hall effect in percolating ferromagnetic granular metal-insulator films," *Applied Physics Letters*, vol. 67, pp. 3497–3499, 1995.

[3] X. X. Zhang, C. Wan, H. Liu, Z. Q. Li, P. Sheng, and J. J. Lin, "Giant Hall effect in nonmagnetic granular metal films," *Physical Review Letters*, vol. 86, no. 24, pp. 5562–5565, 2001.

[4] Y. Hamanaka, K. Fukuta, A. Nakamura, L. M. Liz-Marzán, and P. Mulvaney, "Enhancement of third-order nonlinear optical susceptibilities in silica-capped Au nanoparticle films with very high concentrations," *Applied Physics Letters*, vol. 84, no. 24, pp. 4938–4940, 2004.

[5] Q. Wang, S. Wang, W. Hang, and Q. Gong, "Optical resonant absorption and third-order nonlinearity of (Au,Ag)-TiO_2 granular composite films," *Journal of Physics D*, vol. 38, no. 3, pp. 389–391, 2005.

[6] M. Maaza, O. Nemraoui, C. Sella, A. C. Beye, and B. Baruch-Barak, "Thermal induced tunability of surface plasmon resonance in Au-VO_2 nano-photonics," *Optics Communications*, vol. 254, no. 1–3, pp. 188–195, 2005.

[7] K. D. Cummings, J. C. Garland, and D. B. Tanner, "Optical properties of a small-particle composite," *Physical Review B*, vol. 30, no. 8, pp. 4170–4182, 1984.

[8] I. Tanahashi, Y. Manabe, T. Tohda, S. Sasaki, and A. Nakamura, "Optical nonlinearities of Au/SiO_2 composite thin films prepared by a sputtering method," *Journal of Applied Physics*, vol. 79, no. 3, pp. 1244–1249, 1996.

[9] A. K. Sharma, J. F. Muth, A. Kvit, J. Narayan, and R. M. Kolbas, "Optical and structural characteristics of gold nanocrystallites embedded in a dielectric matrix," in *Proceedings of the Materials Research Society Symposium J*, vol. 617, Boston, Mass, USA, November 2000, 2.7.1.

[10] A. Polman, E. Snoeks, G. N. van den Hoven, et al., "Ion beam synthesis of planar opto-electronic devices," *Nuclear Instruments and Methods in Physics Research B*, vol. 106, no. 1–4, pp. 393–399, 1995.

[11] X. Batlle and A. Labarta, "Finite-size effects in fine particles: magnetic and transport properties," *Journal of Physics D*, vol. 35, no. 6, pp. R15–R42, 2002.

[12] S. Stavroyiannis, I. Panagiotopoulos, D. Niarchos, J. A. Christodoulides, Y. Zhang, and G. C. Hadjipanayis, "New CoPt/Ag films for high density recording media," *Journal of Applied Physics*, vol. 85, pp. 4304–4306, 1999.

[13] M. Yu, Y. Liu, A. Moser, D. Weller, and D. J. Sellmyer, "Nanocomposite CoPt:C films for extremely high-density recording," *Applied Physics Letters*, vol. 75, no. 25, pp. 3992–3994, 1999.

[14] T. Morikawa, M. Suzuki, and Y. Taga, "Soft magnetic properties of Co-Cr-O granular films," *Journal of Applied Physics*, vol. 83, pp. 6664–6666, 1998.

[15] S. Mitani, H. Fujimori, K. Takanashi, et al., "Tunnel-MR and spin electronics in metal-nonmetal granular systems," *Journal of Magnetism and Magnetic Materials*, vol. 198-199, pp. 179–184, 1999.

[16] B. J. Hattink, A. Labarta, M. García del Muro, X. Batlle, F. Sánchez, and M. Varela, "Competing tunneling and capacitive paths in Co-ZrO_2 granular thin films," *Physical Review B*, vol. 67, no. 3, Article ID 033402, 4 pages, 2003.

[17] I. Hrianca, C. Caizer, and Z. Schlett, "Dynamic magnetic behavior of Fe_3O_4 colloidal nanoparticles," *Journal of Applied Physics*, vol. 92, no. 4, pp. 2125–2132, 2002.

[18] C. D. Lorenz and R. M. Ziff, "Precise determination of the critical percolation threshold for the three-dimensional 'Swiss cheese' model using a growth algorithm," *Journal of Chemical Physics*, vol. 114, no. 8, pp. 3659–3661, 2001.

Hindawi Publishing Corporation
Journal of Nanomaterials
Volume 2008, Article ID 352871, 6 pages
doi:10.1155/2008/352871

Review Article

Biologically Inspired Synthesis Route to Three-Dimensionally Structured Inorganic Thin Films

Birgit Schwenzer[1, 2] and Daniel E. Morse[1, 2, 3]

[1] *Institute for Collaborative Biotechnologies, University of California, Santa Barbara, CA 93106-5100, USA*
[2] *California NanoSystems Institute, University of California, Santa Barbara, CA 93106-5100, USA*
[3] *Department of Molecular Cellular and Developmental Biology, University of California, Santa Barbara, CA 93106-9610, USA*

Correspondence should be addressed to Prof. Daniel E. Morse, d_morse@lifesci.ucsb.edu

Received 2 October 2007; Accepted 26 December 2007

Recommended by Ping Xiao

Inorganic thin films (hydroxide, oxide, and phosphate materials) that are textured on a submicron scale have been prepared from aqueous metal salt solutions at room temperature using vapor-diffusion catalysis. This generic synthesis approach mimics the essential advantages of the catalytic and structure-directing mechanisms observed for the formation of silica skeletons of marine sponges. Chemical composition, crystallinity, and the three-dimensional morphology of films prepared by this method are extremely sensitive to changes in the synthesis conditions, such as concentrations, reaction times, and the presence and nature of substrate materials. Focusing on different materials systems, the reaction mechanism for the formation of these thin films and the influence of different reaction parameters on the product are explained.

1. INTRODUCTION

Nanostructured thin films as well as thin films with no surface texture are currently used for many applications such as electro-optical devices [1], batteries [2], solar cell technology [3], and gas sensors [4]. These applications require high purity, defect-free materials. The use of metal organic chemical vapor deposition (MOCVD), molecular-beam epitaxy (MBE), or liquid-phase epitaxy (LPE) techniques represents the state-of-the-art fabrication processes for such high-quality semiconductor thin films.

However, in recent years, lower-cost approaches to fabricate these films have emerged, among them hydrothermal [5] and electrochemical [6] synthesis methods. In addition, synthesis techniques that mimic biomineralization processes have received much attention because of the inherently benign and malleable conditions under which biominerals are produced. An increasing number of research groups have been studying biomimetic [7] or biologically inspired [8] pathways towards preparation of semiconductor materials in the past few years using biological principles of materials formation.

Biomineralization, including the formation of bones, teeth, shells, or the silica skeletons of marine sponges, takes place in vivo under ambient conditions. These biomineralization processes often produce highly ordered structures on the nanoscopic as well as the macroscopic scale, and generally nano- or micrometer-sized defects within these structures do not propagate, but are corrected on a short-range scale. The lessons learned from these biomimetic systems follow a general model [9, 10]: the reaction environment is anisotropically preorganized; this provides a framework from which the material can grow in an anisotropic manner. Kinetic control is imposed at the stage of nucleation, typically at an interface in the reaction environment, by closely controlling the supply of molecular precursor chemicals. In addition, crystal growth is vectorially regulated by a template, as seen both in natural systems [11–13] and artificial systems such as those based on virus protein coats [14], ferritin-like cage proteins [14, 15], and others [16].

Based on previous research in our group on silicatein (for *silica protein*) [13, 17, 18], an enzymatic biocatalyst discovered in the biologically fabricated needles of silica made by a sponge (*Tethya Aurantia*), we used these biomimetic

concepts for the development of a bioinspired synthesis route to nanostructured inorganic materials.

We observed that silicification in *Tethya Aurantia* is controlled by occluded protein filaments (silicateins) that serve as both templates and catalysts for the deposition of opal-like SiO_2 [17–19]. In vitro experiments with isolated silicatein filaments yielded SiO_2 nanoparticles similar to those formed in vivo, when the proteins were exposed to silicon tetraethoxide (TEOS) [18]. Recognizing silicatein to be a specialized member of the superfamily of hydrolytic enzymes [17, 18], Zhou et al. used site-directed mutagenesis to confirm the proposition that the sidechains of two specific amino acids, serine and histidine, play an essential role as partners in the catalytically active center of silicatein [19]. Based on these findings, the following mechanism for the formation of SiO_2 was proposed [18]: resulting from the close proximity of the hydroxyl group of the serine, the hydrogen atom of this functional group becomes a bridging hydrogen atom linking the oxygen atom of the hydroxyl group and the nitrogen atom in the 3 positions of the imidazole ring on the histidine. This partial withdrawal of the proton leads to an increased nucleophilicity of the oxygen atom on the serine, facilitating a nucleophilic addition onto the electron-deficient silicon center of TEOS. An EtO^- group is cleaved from the TEOS precursor, reacting with the electron-deficient bridging hydrogen to form EtOH, and the addition of a water molecule then initiates hydrolysis to yield silanol, with restoration of the enzyme's catalytic center with its $–CH_2–O\cdots H\cdots N–$ bond. Subsequently either further hydrolysis takes place, or several silicon alkoxide molecules react via condensation to form SiO_2 as the final product [18].

Mimicking this hydrolysis/condensation mechanism with its $–CH_2–O\cdots H\cdots N–$ sequence as the reactive center for catalysis, silica, silsesquioxanes, and metal oxide materials has been prepared using block copolypeptides of the essential catalytic amino acids [20] or small functionalized molecules [21] in an effort to remove the biomolecule from the process. In a further translation step, self-assembled monolayers (SAMs) of suitable hydroxyl- and imidazole-terminated molecules have been patterned on gold-coated silicon wafers [22]. Similarly, the same catalytic activity has been achieved by functionalizing gold nanoparticles with the respective surface coating to mimic the catalytic center of silicatein [23]. While these approaches were successful for the preparation of a variety of metal oxide materials, such as TiO_2 [24] and Ga_2O_3 [25], the use of an organic template to direct synthesis is not feasible for device applications due to the contamination of the end product with the remnants of the organic template. Removing the organic elements from the process would alleviate this source of contamination and can potentially yield high-purity materials.

Translating these biomimetic systems further to achieve carbon-free reaction conditions, we recently reported a kinetically-controlled vapor-diffusion catalysis method as a biologically-inspired synthesis approach to hierarchically-structured inorganic thin film preparation [26–29]. This method uses the principles of slow catalysis and vectorial control to achieve anisotropic, kinetically-controlled reaction conditions. However, unlike the previously mentioned approaches, the aqueous reaction solution and the gaseous catalyst ensure an extremely low level of contamination for this general method to fabricate metal oxide, hydroxide, and phosphate thin films. Other groups [30, 31] have reported the same type of structured thin films or nucleation on substrates using chemical bath deposition (CBD). In contrast to our work, substrates are essential in those methods to nucleate the films, and in some cases organic solvents are used as part of the precursor-containing solution. We here summarize and cross-link previously reported results from our group and others, and describe in more detail the mechanism for the formation of substrate-free, unsupported films and the influence of different reaction parameters on the resulting thin film products.

2. VAPOR-DIFFUSION CATALYSIS

A wide variety of inorganic materials in thin film morphology have been prepared using vapor-diffusion catalysis [26–29] or CBD [30, 32]. For growth on substrates, a heterogeneous nucleation mechanism has been established. Figure 1 shows an illustration of the experimental setup for a typical vapor-diffusion catalysis reaction.

In the vapor-diffusion catalysis method, a gaseous catalyst from an external source is diffused into an aqueous metal salt solution (Figure 1(a)). Adding the catalyst as a gas at low concentrations by vapor-diffusion instead of adjusting the pH homogeneously in solution leads to an anisotropic reaction environment that is temporally and spatially controlled by the rate of diffusion. In the case illustrated and described above, a pH gradient, decreasing from the vapor-liquid interface towards the bottom of the reaction vessel, is created.

Rather than introducing the gaseous catalyst into the closed reaction environment by connecting it to a gas cylinder, we rely on the in situ formation of a liquid/vapor solution equilibrium from a suitable source to saturate the reaction chamber with gaseous catalyst. For example, an aqueous NH_4OH solution is used to yield an NH_3 atmosphere (Figure 1(a)), which serves as the catalyst for the reactions discussed here. Employing an environment that from the beginning is completely saturated with the catalytic gas would significantly accelerate the initial rates of hydrolysis, condensation and nucleation, and therefore would not allow the maximum benefits of slow catalysis that we achieve through vapor-diffusion catalysis as opposed to, for example, hydrothermal reactions.

The slow diffusion and catalysis allow for very localized formation of nucleation crystallites close to the meniscus of the reaction solution during the first minutes of the synthesis. Measurements of pH changes at the vapor-liquid interface have confirmed that the increase in pH, that is, $[OH^-]$ concentration, can be correlated with the formation of nucleation crystallites [27]. Figures 1(b)–1(d) show SEM images of $Co_5(OH)_8(NO_3)_2\cdot 2H_2O$ films at various stages of formation. After 15 minutes, clusters that seem to originate from discrete island nucleation can be observed. The shape of the crystallites growing into the aqueous reaction solution (indicated by the arrow in Figure 1(b)) is similar to the spindle-shaped hexagonal crystallites Yamabi and Imai [31] observed

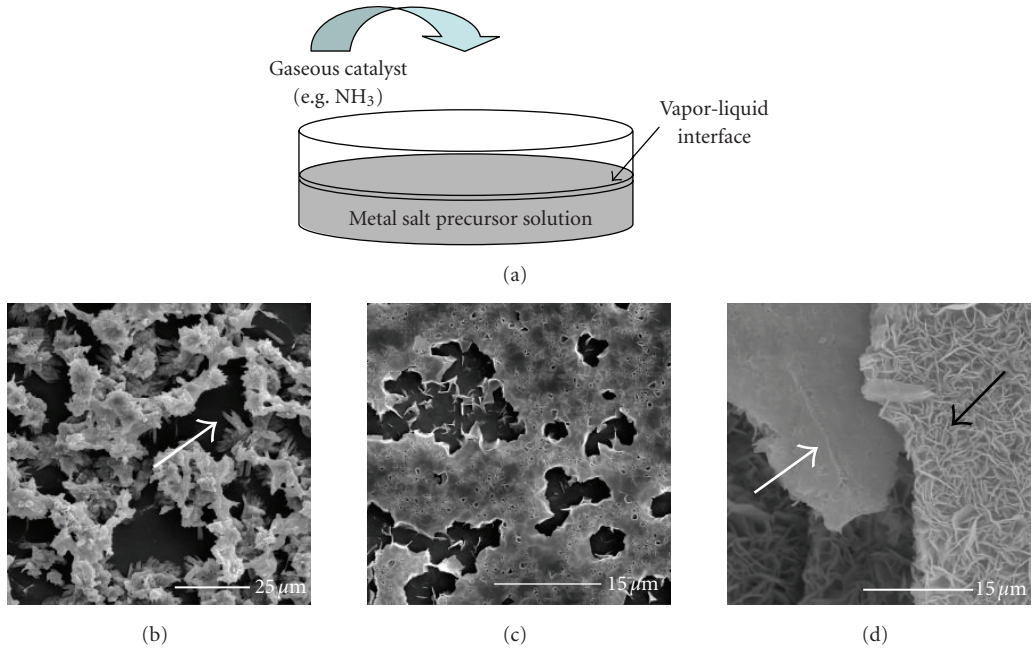

Figure 1: (a) Schematic illustration of the vapor-diffusion catalysis method for unsupported film formation from aqueous metal salt solutions; SEM images of the growth of $Co_5(OH)_8(NO_3)_2 \cdot 2H_2O$ from 0.1 M $Co(NO_3)_2$ solution showing (b) noncontinuous network of partially fused $Co_5(OH)_8(NO_3)_2 \cdot 2H_2O$ nucleation islands after 15 minute reaction time, (c) extended network of further fused $Co_5(OH)_8(NO_3)_2 \cdot 2H_2O$ nucleation islands after 30-minute reaction time; and (d) fully condensed structured $Co_5(OH)_8(NO_3)_2 \cdot 2H_2O$ thin films after 60-minute reaction time.

for their CBD growth on glass, Si, and other substrates. Some fusion of these crystallites, originating from their nucleation centers rather than the protruding crystalline spikes, can already be seen. Thirty minutes after the start of the reaction, the formation of a continuous although still porous plane connecting the individual crystallites has progressed significantly (Figure 1(c)). This plane will eventually form the backplane of the structured film, thickening to ~1.5 μm [26] and incorporating the original spindle-like crystallites into the base of the film. For the formation of structured $Co_5(OH)_8(NO_3)_2 \cdot 2H_2O$ thin films from a 0.1 M $Co(NO_3)_2$ solution, the fusion of the backplane is complete after ~60 minutes; simultaneously during this time, plates with a thickness of ~30–50 nm [26] formed protruding orthogonally from the continuous backplane oriented into the aqueous reaction solution (Figure 1(d)). The arrows in Figure 1(d) indicate the backplane (white arrow) and the nanostructured side of the material (black arrow), respectively.

Hydrothermal methods, that rely on the in situ formation of either one of the precursor materials or the reaction catalyst, similarly achieve a temporally controlled slow crystal formation [30, 33]. For example, thermal decomposition of urea [30] or hexamethylenetetramine (HMT) [33] has been used to liberate a basic catalyst. However, this approach does not make use of spatial control of nucleation. The reaction environment in hydrothermal synthesis is isotropic, with homogeneous nucleation in solution competing with heterogeneous nucleation on the supplied substrate.

The density, size, and shape of the structures protruding from the continuous backplane of inorganic films prepared using vapor-diffusion catalysis can be modified without the use of organic surfactants or growth inhibitors. We have shown this control to depend on the type and concentration of the metal salt precursor and gaseous catalyst and on the reaction time [26, 27].

As can be seen in Figure 2, the morphology and shape of the nanostructured features and their 3-dimensionality vary depending on the chemical composition of the final products. Both materials (ZnO, Figure 2(a); $Zn_5(OH)_8(NO_3)_2 \cdot 2H_2O$, Figure 2(b)) were prepared by vapor-diffusion catalysis, diffusing ammonia into an aqueous $Zn(NO_3)_2$ solution under differing conditions of precursor concentration and reaction time [26, 27].

The nanostructured ZnO film seen in Figure 2(a) was crystallized by vapor-diffusion catalysis from a 0.05 M $Zn(NO_3)_2$ solution, whereas the $Zn(NO_3)_2$ concentration used to obtain the structured $Zn_5(OH)_8(NO_3)_2 \cdot 2H_2O$ film (Figure 2(b)) was twice as high. With the slower nucleation rate, hexagonal ZnO is formed [27]. In contrast, the rate of initial nucleation is faster when higher concentrations of metal salt precursor solution and gaseous catalyst are used, leading to the incorporation of anionic counterions from the precursor material. To accommodate the incorporation of bulky NO_3^- ions, the films that are formed from the higher concentration of $Zn(NO_3)_2$ precursor do not crystallize in a close-packed hexagonal crystal structure, instead a layered hydrotalcite-like structure is formed [26, 34]. This interesting structure consists of Zn^{2+} containing layers, that carry a net positive charge from the incorporation of tetrahedrally coordinated Zn^{2+} ions into the crystal structure of otherwise

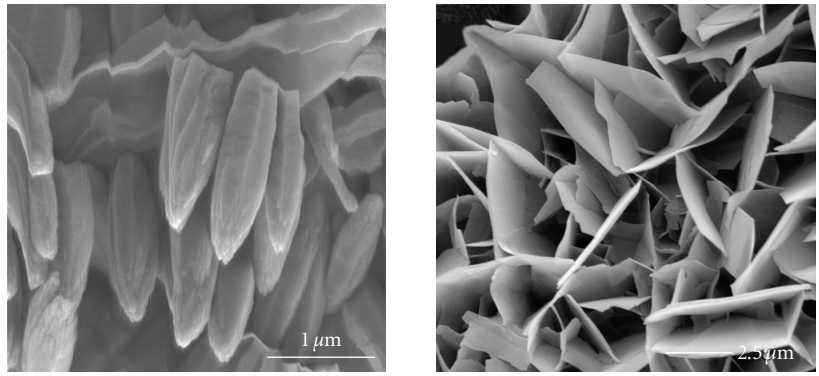

(a) (b)

Figure 2: (a) High-resolution SEM image of the nanostructures protruding from a ZnO thin film prepared by low-concentration vapor-diffusion from a 0.05 M $Zn(NO_3)_2$ solution. Reprinted by permission from *Journal of the American Chemical Society*, vol. 128, no. 31, pp. 10276–10280, 2006©American Chemical Society. (b) SEM image of the nanostructures protruding from a $Zn_5(OH)_8(NO_3)_2 \cdot 2H_2O$ thin film prepared by vapor-diffusion from a 0.1 M $Zn(NO_3)_2$ solution.

octahedrally coordinated ions [34]. The layers are held together by the intercalation of NO_3^- counterions, resulting in a $Zn^{2+} : NO_3^-$ ratio of 5 : 2. The overall crystal structure of this layered compound is monoclinic [35]. We believe that the difference in nanostructured morphologies of the two materials is a direct consequence of the difference in their crystal structures. Further experiments to confirm this hypothesis are in progress.

To study the effect on crystallinity and morphology of films prepared using vapor-diffusion catalysis when substrates are introduced into the reaction system, different substrates were used as templates for the growth of thin films from aqueous $Zn(NO_3)_2$ solutions [28]. Unlike the results of CBD [32], again the reaction solution only contained the metal salt precursor and the catalyst was added by diffusion as a gaseous medium. The reaction solution was not stirred during the synthesis to not disturb the anisotropic reaction environment.

Two examples of structured thin films grown from the same 0.1 M $Zn(NO_3)_2$ solution can be seen in Figure 3. The observed difference in morphology in this case is not due to different reaction conditions but to nucleation sites provided by different substrates that offer a more or less suitably lattice-matched base for ZnO [28]. The film in Figure 3(a) has been grown on an amorphous glass substrate and consists of amorphous $Zn_5(OH)_8(NO_3)_2 \cdot 2H_2O$. The 3-dimensional structure of the film with its individual plates protruding from the backplane attached to the nucleation surface closely resembles that of the unsupported $Zn_5(OH)_8(NO_3)_2 \cdot 2H_2O$ films (Figure 2(b)). When polished (0001) oriented epitaxially grown ZnO was used as substrate, the difference of this substrate in crystallinity, crystallographic lattice matching with respect to $Zn_5(OH)_8(NO_3)_2 \cdot 2H_2O$ and ZnO, and the polycrystalline versus epitaxially grown surface morphology evidently suppressed the nucleation of $Zn_5(OH)_8(NO_3)_2 \cdot 2H_2O$ in favor of the formation of a 3-dimensional network of highly crystalline ZnO [28]. These results indicate that substrates of different chemical composition and degrees of crystallinity can be used to induce the preferential growth of specific materials and govern the morphology of the resulting thin films. Furthermore, the integrability of our vapor-diffusion synthesis method into existing manufacturing processes such as MOCVD or MBE has been demonstrated, and these results confirm its potential use as a low-cost alternative to these fabrication methods.

Another way to modify the chemical composition of structured thin films prepared by vapor-diffusion catalysis is to supply different counterions to be incorporated into the crystal structure. This method allows subtle changes to be made in the crystal structure, such as replacing the anions that hold together the positively charged metal ion sheets in hydrotalcite-like structures, and to thereby change the lattice spacing along the *c*-direction within the polycrystalline material. For example, $Co_5(OH)_8(NO_3)_2 \cdot 2H_2O$, $Co_5(OH)_8SO_4 \cdot 2H_2O$, and $Co_5(OH)_8Cl_2 \cdot 3H_2O$ have been prepared from their respective metal nitrate, sulfate, and chloride salts, with diffraction analyses confirming changes in the lattice spacing proportional to the counterion diameter [26]. While the rates of formation of the hierarchically structured films of these cobalt-containing hydrotalcite-like materials vary slightly, their overall morphologies are very similar. This is another indication that similar crystal structures favor the formation of similar types of nanostructures that grow from the continuous backplane of the thin film material.

The chemical composition of thin films can be changed more significantly, when additional anions are added to the reaction solution. If the incorporation of these anions is more favorable than the formation of hydroxide or oxide materials, different types of inorganic materials can be formed using the vapor-diffusion catalysis method. As one example, we have identified synthesis conditions that favor the formation of metal phosphate thin films under very similar conditions than have been used to prepare the metal oxide or hydroxide films [26, 29]. Thus, we found that the addition of $(NH_4)_2HPO_4$ to aqueous chromium or manganese salt

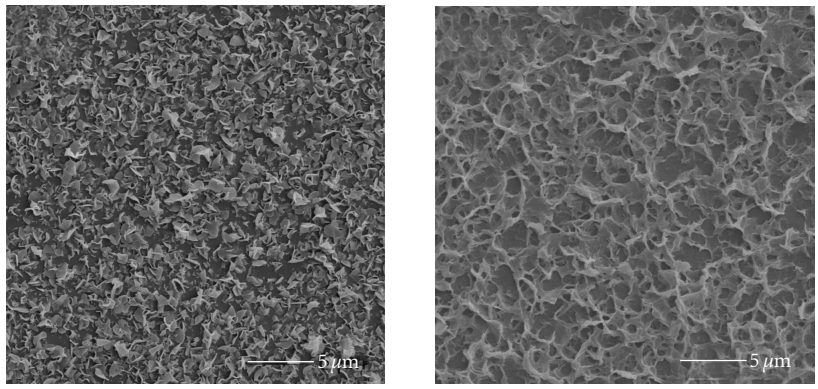

(a) (b)

Figure 3: SEM images of thin films grown on different substrates from an aqueous 0.1 M $Zn(NO_3)_2$ solution by vapor-diffusion catalysis over the course of 6 hours: (a) $Zn_5(OH)_8(NO_3)_2 \cdot 2H_2O$ on amorphous glass; (b) ZnO on the (0001) face of epitaxially grown ZnO.

solutions leads to the formation of $CrPO_4 \cdot 6H_2O$ [29] and $Mn_3(PO_4)_2 \cdot 7H_2O$ [26], respectively. These films also display the same general morphology as described above, with submicron-scale structures protruding from the side of the continuous film that had been facing the aqueous solution during the 18–24 hour reaction time.

3. CONCLUSION

A generic low-temperature method, for the preparation of structured inorganic metal oxide, hydroxide and phosphate films, has been introduced. The underlying biomimetic principles of materials formation have been reviewed, and their importance has been discussed. Because the chemical composition, crystallinity and morphology of the films, is very susceptible to changes in the reaction environment, this opens many possibilities to tailor the properties of films prepared by this environmentally benign vapor-diffusion catalysis. The method allows the synthesis of freestanding, unsupported films as well as film growth on substrates. We have proposed a nucleation sequence for the formation of structured films grown by this kinetically-controlled synthesis approach, and discussed previously reported results, cross-linking the findings and discussing different possibilities for modification of selected aspects of thin film growth.

In summary, we have reviewed a generic synthesis approach for low-cost, low-temperature fabrication of structured inorganic metal oxide, hydroxide and phosphate films. The integrability of the vapor-diffusion catalysis method into existing manufacturing processes such as MOCVD or MBE has been demonstrated.

ACKNOWLEDGMENTS

This work was supported in part by grants from the U.S. Department of Energy (DEFG03-02ER46006); DARPA (HR0011-04-1-0059); the U.S. Army Research Office through Grant no. DAAD19-03-D-0004 to the Institute for Collaborative Biotechnologies; and the MRSEC Program (Award no. DMR05-20415) of the National Science Foundation (UCSB Materials Research Laboratory).

REFERENCES

[1] Y. A. Vlasov, X.-Z. Bo, J. C. Sturm, and D. J. Norris, "On-chip natural assembly of silicon photonic bandgap crystals," *Nature*, vol. 414, no. 6861, pp. 289–293, 2001.

[2] L. Kavan, M. Kalbáč, M. Zukalová, et al., "Lithium storage in nanostructured TiO_2 made by hydrothermal growth," *Chemistry of Materials*, vol. 16, no. 3, pp. 477–485, 2004.

[3] M. C. Lux-Steiner, A. Ennaoui, C.-H. Fischer, et al., "Processes for chalcopyrite-based solar cells," *Thin Solid Films*, vol. 361-362, pp. 533–539, 2000.

[4] S. Marian, D. Tsiulyanu, T. Marian, and H.-D. Liess, "Chalcogenide-based chemical sensors for atmospheric pollution control," *Pure and Applied Chemistry*, vol. 73, no. 12, pp. 2001–2004, 2001.

[5] J. H. Kim, E.-M. Kim, D. Andeen, D. Thomson, S. P. DenBaars, and F. F. Lange, "Growth of heteroepitaxial ZnO thin films on GaN-buffered Al_2O_3 (0001) substrates by low-temperature hydrothermal synthesis at 90°C," *Advanced Functional Materials*, vol. 17, no. 3, pp. 463–471, 2007.

[6] D. M. Soolaman and H.-Z. Yu, "Monolayer-directed electrodeposition of oxide thin films: surface morphology versus chemical modification," *Journal of Physical Chemistry C*, vol. 111, no. 38, pp. 14157–14164, 2007.

[7] Q. Dong, H. Su, W. Cao, D. Zhang, Q. Guo, and F. Zhang, "Assembly and formation of biomorphic tin dioxide by a biomimetic sol-gel approach involving glycoprotein," *European Journal of Inorganic Chemistry*, vol. 2007, no. 16, pp. 2265–2273, 2007.

[8] M. A. Stroscio and M. Dutta, "Biologically-inspired chemically-directed self-assembly of semiconductor quantum-dot-based systems: phonon-hole scattering in DNA bound to DNA-quantum-dot complexes," *International Journal of High Speed Electronics and Systems*, vol. 16, no. 2, pp. 659–668, 2006.

[9] S. Mann, *Biomineralization: Principles and Concepts in Bioinorganic Materials Chemistry*, Oxford University Press, Oxford, UK, 2001.

[10] S. Mann, *Biomimetic Materials Chemistry*, VCH, New York, NY, USA, 1996.

[11] G. Falini, S. Albeck, S. Weiner, and L. Addadi, "Control of aragonite or calcite polymorphism by mollusk shell macromolecules," *Science*, vol. 271, no. 5245, pp. 67–69, 1996.

[12] X. Su, A. M. Belcher, C. M. Zaremba, D. E. Morse, G. D. Stucky, and A. H. Heuer, "Structural and microstructural characterization of the growth lines and prismatic microarchitecture in red abalone shell and the microstructures of abalone "flat pearls"," *Chemistry of Materials*, vol. 14, no. 7, pp. 3106–3117, 2002.

[13] H. Cölfen and S. Mann, "Higher-order organization by mesoscale self-assembly and transformation of hybrid nanostructures," *Angewandte Chemie International Edition*, vol. 42, no. 21, pp. 2350–2365, 2003.

[14] C. Mao, D. J. Solis, B. D. Reiss, et al., "Virus-based toolkit for the directed synthesis of magnetic and semiconducting nanowires," *Science*, vol. 303, no. 5655, pp. 213–217, 2004.

[15] M. Allen, D. Willits, M. Young, and T. Douglas, "Constrained synthesis of cobalt oxide nanomaterials in the 12-subunit protein cage from Listeria innocua," *Inorganic Chemistry*, vol. 42, no. 20, pp. 6300–6305, 2003.

[16] H. Aldersey-Williams, "Towards biomimetic architecture," *Nature Materials*, vol. 3, no. 5, pp. 277–279, 2004.

[17] K. Shimizu, J. Cha, G. D. Stucky, and D. E. Morse, "Silicatein α: cathepsin L-like protein in sponge biosilica," *Proceedings of the National Academy of Sciences of the United States of America*, vol. 95, no. 11, pp. 6234–6238, 1998.

[18] J. N. Cha, K. Shimizu, Y. Zhou, et al., "Silicatein filaments and subunits from a marine sponge direct the polymerization of silica and silicones in vitro," *Proceedings of the National Academy of Sciences of the United States of America*, vol. 96, no. 2, pp. 361–365, 1999.

[19] Y. Zhou, K. Shimizu, J. N. Cha, G. D. Stucky, and D. E. Morse, "Efficient catalysis of polysiloxane synthesis by silicatein α requires specific hydroxy and imidazole functionalities," *Angewandte Chemie International Edition*, vol. 38, no. 6, pp. 779–782, 1999.

[20] J. N. Cha, G. D. Stucky, D. E. Morse, and T. J. Deming, "Biomimetic synthesis of ordered silica structures mediated by block copolypeptides," *Nature*, vol. 403, no. 6767, pp. 289–292, 2000.

[21] K. M. Roth, Y. Zhou, W. Yang, and D. E. Morse, "Bifunctional small molecules are biomimetic catalysts for silica synthesis at neutral pH," *Journal of the American Chemical Society*, vol. 127, no. 1, pp. 325–330, 2005.

[22] D. Kisailus, Q. Truong, Y. Amemiya, J. C. Weaver, and D. E. Morse, "Self-assembled bifunctional surface mimics an enzymatic and templating protein for the synthesis of a metal oxide semiconductor," *Proceedings of the National Academy of Sciences of the United States of America*, vol. 103, no. 15, pp. 5652–5657, 2006.

[23] D. Kisailus, M. Najarian, J. C. Weaver, and D. E. Morse, "Functionalized gold nanoparticles mimic catalytic activity of a polysiloxane-synthesizing enzyme," *Advanced Materials*, vol. 17, no. 10, pp. 1234–1239, 2005.

[24] J. L. Sumerel, W. Yang, D. Kisailus, J. C. Weaver, J. H. Choi, and D. E. Morse, "Biocatalytically templated synthesis of titanium dioxide," *Chemistry of Materials*, vol. 15, no. 25, pp. 4804–4809, 2003.

[25] D. Kisailus, J. H. Choi, J. C. Weaver, W. Yang, and D. E. Morse, "Enzymatic synthesis and nanostructural control of gallium oxide at low temperature," *Advanced Materials*, vol. 17, no. 3, pp. 314–318, 2005.

[26] B. Schwenzer, K. M. Roth, J. R. Gomm, M. Murr, and D. E. Morse, "Kinetically controlled vapor-diffusion synthesis of novel nanostructured metal hydroxide and phosphate films using no organic reagents," *Journal of Materials Chemistry*, vol. 16, no. 4, pp. 401–407, 2006.

[27] D. Kisailus, B. Schwenzer, J. Gomm, J. C. Weaver, and D. E. Morse, "Kinetically controlled catalytic formation of zinc oxide thin films at low temperature," *Journal of the American Chemical Society*, vol. 128, no. 31, pp. 10276–10280, 2006.

[28] B. Schwenzer, J. R. Gomm, and D. E. Morse, "Substrate-induced growth of nanostructured zinc oxide films at room temperature using concepts of biomimetic catalysis," *Langmuir*, vol. 22, no. 24, pp. 9829–9831, 2006.

[29] J. R. Gomm, B. Schwenzer, and D. E. Morse, "Textured films of chromium phosphate synthesized by low-temperature vapor diffusion catalysis," *Solid State Sciences*, vol. 9, no. 5, pp. 429–431, 2007.

[30] E. Hosono, S. Fujihara, I. Honma, and H. Zhou, "Fabrication of morphology and crystal structure controlled nanorod and nanosheet cobalt hydroxide based on the difference of oxygen-solubility between water and methanol, and conversion into Co_3O_4," *Journal of Materials Chemistry*, vol. 15, no. 19, pp. 1938–1945, 2005.

[31] S. Yamabi and H. Imai, "Growth conditions for wurtzite zinc oxide films in aqueous solutions," *Journal of Materials Chemistry*, vol. 12, no. 12, pp. 3773–3778, 2002.

[32] G. Hodes, "Semiconductor and ceramic nanoparticle films deposited by chemical bath deposition," *Physical Chemistry Chemical Physics*, vol. 9, no. 18, pp. 2181–2196, 2007.

[33] T. Zhang, W. Dong, M. Keeter-Brewer, S. Konar, R. N. Njabon, and Z. R. Tian, "Site-specific nucleation and growth kinetics in hierarchical nanosyntheses of branched ZnO crystallites," *Journal of the American Chemical Society*, vol. 128, no. 33, pp. 10960–10968, 2006.

[34] W. Stählin and H. R. Oswald, "The crystal structure of zinc hydroxide nitrate, $Zn_5(OH)_8(NO_3)_2 \cdot 2H_2O$," *Acta Crystallographica. Section B*, vol. 26, no. 6, pp. 860–863, 1970.

[35] JCPDS file # 01-072-0627.

Hindawi Publishing Corporation
Journal of Nanomaterials
Volume 2008, Article ID 736534, 6 pages
doi:10.1155/2008/736534

Research Article

Chromium-Induced Nanocrystallization of a-Si Thin Films into the Wurtzite Structure

K. Uma Mahendra Kumar and M. Ghanashyam Krishna

School of Physics, University of Hyderabad, Hyderabad-500 046, India

Correspondence should be addressed to M. Ghanashyam Krishna, mgksp@uohyd.ernet.in

Received 30 October 2007; Accepted 4 February 2008

Recommended by Robert Dorey

Chromium metal-induced nanocrystallization of amorphous silicon (a-Si) thin films is reported. The nanocrystalline nature of these films is confirmed from X-ray diffraction and Raman spectroscopy. Significantly, the deconvolution of Raman spectra reveals that the thin films were crystallized in a mixed phase of cubic diamond and wurzite structure as evidenced by the lines at 512 and 496 cm^{-1}, respectively. The crystallite sizes were between 4 to 8 nm. Optical properties of the crystallized silicon, derived from spectral transmittance curves, revealed high transmission in the region above the band gap. Optical band gap varied between 1.3 to 2.0 eV depending on the nature of crystallinity of these films and remained unaltered with increase in Cr addition from 5 to 30%. This signifies that the electronic structure of the nanocrystalline Silicon films is not affected considerably inspite of the presence of metal silicides and the process of crystallization.

1. INTRODUCTION

In recent years, nanocrystalline silicon has found substantial applications in a variety of areas including visible electroluminescent devices [1–3] field-induced ballistic electron emitter [4], thermally induced ultrasonic emitter [5], and biocompatible scaffold [6] to name a few. Nanocrystallization in a-Si has been achieved by different methods starting from solid phase crystallization (SPC) [7], excimer laser annealing [8] and metal induced crystallization (MIC) [9].

Silicon crystallizes in the cubic diamond structure under ambient conditions. However, it is also known to have several polymorphs that are stable only at high pressures. Hexagonal-wurtzite silicon is one such structure and there have been very few reports in literature on its stabilization either in bulk or thin form at ambient pressure and temperature conditions [10]. The Raman spectra of these stabilized structures are studied but very little is known about the optical properties such as transmission, refractive indexand optical band gap of the wurtzite structured Si films.

Chromium-induced nanocrystallization of silicon has been very sparsely reported previously although crystallization induced by metals such as Al and Ni has been extensively reported [11–13]. It is known that in many silicides the metal-silicon bond length is very similar to that of Si-Si bond lengths in the wurtzite structure [14]. Furthermore, in the process of metal-induced crystallization of Si, both the metal and metal silicides that form as a consequence of the thermal treatment, act as nucleating agents for the crystallization of Si. The eventual structure of the Si nanocrystals, then, closely mimics that of the metal silicide. The choice of Cr was, therefore, based on the premise that its silicides under favourable thermodynamic conditions could result in the formation of the wurtzite structure.

The objectives of the present work are therefore to study the possibility of stabilizing the wurtzite structure of Si in thin film form by the metal-induced nanocrystallization route. A further objective is to study the optical properties such as spectral transmission, refractive index, and optical band gap of the wurtzite form of silicon thin films.

2. EXPERIMENTAL

Thin films of Cr/a-Si/Borosilicate Glass (BSG) substrate stacks are deposited by resistive thermal evaporation. Silicon thin films were grown by evaporating granular silicon

powder (99.99% pure) from a tantalum boat on to BSG substrates. In order to deposit Cr films, Chromium (99.99% pure), shots were sublimed from a Tantalum boat. The vacuum chamber was evacuated using a diffusion-rotary pump combination equipped with a liquid nitrogen trap to a base pressure of 1×10^{-6} Torr. In all cases, the substrate to source distance was kept constant at 8 cm. Relative concentration of metal in the a-Si matrix were varied while varying the a-Si thickness; in the case of Cr/a-Si/BSG system, the Cr concentration was varied from 5% to 30% by varying the a-Si thin film thickness from 600 nm to 100 nm. After recording the spectral transmission curves, these films were subjected to thermal annealing. The Cr/a-Si/BSG stacks were annealed at 500°C for 20 minutes. The thickness was measured in situ by a quartz crystal monitor and after deposition using a surface profilometer (Model XP-1 Ambios Tech.,USA) and also was calculated from the spectral transmission curves [15]. Before and after annealing, the films was characterized for transmission in the wavelength range 350 to 2500 nm by means of a dual-beam spectrophotometer (UV-VIS-NIR, Model, Jasco V-570) having a resolution limit of 0.2 nm and a sampling interval of 2 nm. The transmitted intensities were measured at accuracy better than 0.3%. The refractive indices were extracted from the measured spectral curves by curve fitting using the PUMA code [15]. The Raman spectra were recorded in air using an argon ion laser in the back scattering geometry in a JY-ISA T64000 spectrometer equipped with a confocal microscope and 100X objective ($1\,\mu$m diameter focal spot size). Care was taken to optimize the parameters of the laser, so that it does not induce onset of crystallization in the sample. The phase content with in the samples was investigated in a spectral region 200 to 600 cm^{-1} with an irradiation time of 50 seconds. The Raman spectra presented in this paper are the result of a scan with irradiation duration of 50 seconds. X-ray diffraction patterns were recorded on a powder x-ray diffractometer (CPS120 of Inel, France) machine equipped with a Co K_α = 0.178896 nm and gas phase position sensitive detector.

3. RESULTS AND DISCUSSION

3.1. Morphology and structure

An optical micrograph of a-Si thin film grown on glass by thermal evaporation is shown in Figure 1(a). The observed microstructures are very familiar features in MBE grown epitaxial silicon thin films and are known as shallow saucer pits (S-pits) [16]. These structures have also been interpreted as point defects or clustered crystallographic imperfections. The silicon thin films shown in these images were X-ray amorphous and hence the saucer pits seen in our samples cannot be due to crystallographic imperfection. The possible reasons for this kind of growth in MBE grown silicon thin films were attributed to poor vacuum conditions ($<10^{-7}$ Torr) and low substrate temperatures during deposition (<700°C). According to Pearce and McMahon metal contamination will also cause S-pits [17]. In our case, the films were deposited on substrates held at ambient temperature during deposition and in vacuum of 10^{-6} Torr and these can be the causes for the formation of the S-pits.

Optical microscopy reveals the morphology of the a-Si thin films crystallized by Cr-induced crystallization after annealing at 500°C for 20 minutes Figure 1(b). Different kinds of morphologies have been reported earlier in literature for crystalline Si films. Choi et al. reported disk-like grains, which grow radially upwards on annealing [18], and Yoon et al. observed dendrite-like growth [19]. After annealing the Cr/a-Si/BSG stack at 500°C in a muffle furnace in ambient atmosphere, the morphology is as shown in Figure 1(b) for a film of thickness of 100 nm with a 30 nm of Cr over the a-Si thin film as a blanket layer and for the film of thickness 280 nm with the same thickness of Cr overlayer in Figure 1(c). In the latter case, the Si thin film seems to be melted. Cr interaction with a-Si is important since this kind of stack structure is found in a-Si solar cells [20]. In the present study, after melting, due to the density gradients in crystalline silicon and a-Si, ripple formation occurred. These ripple structures are known in laser ablated silicon samples where silicon melting is evidenced [21, 22]. Levinson reported columnar structures of $CrSi_2$ in the matrix of Si [23]. However, in our case the quantity of $CrSi_2$ is very small compared to the a-Si, and therefore these ripples can be attributed to the crystalline Si.

X-ray diffraction patterns of the annealed samples are shown in Figure 2. The unambiguous identification of the presence of crystalline Si is difficult because there is an overlap with the reflections from the silicides. There are two Bragg reflections at 2θ values of 78.06° and 105.33°, which can be indexed as originating either from Si or $CrSi_2$. To remove the ambiguity, Raman scattering experiments were carried out in both cases and results are presented in the next section. However, crystallite size determination from FWHM shows that the films are nanocrystalline with an average crystallite size of 6 ± 1 nm.

3.2. Raman spectroscopy

The Raman spectrum of a 100 nm thick a-Si film on glass substrate is shown in Figure 3. A broad feature centered at 472 cm^{-1} was observed. After correcting for the base line, a Voigt-like function was used to curve fit the Raman spectra. The curve fitting reveals that the Raman signal between 400 and 560 cm^{-1} is comprised of two resonances, one peak centered at 472 cm^{-1} which is attributed to the amorphous silicon, while the peak at 504 cm^{-1} is due to nanocrystalline cubic silicon. Using the Zi model, the derived crystallite size was estimated $\sim 2 \pm 0.5$ nm size [24]. However, since these films were X-ray amorphous, the values may not be entirely accurate.

In our studies, the relative concentration of Cr metal was varied from 30% to 5% by varying the a-Si film thickness from 100 nm to 600 nm. After annealing the Cr/a-Si/BSG stack at 500°C for 20 minutes, crystallization of a-Si started. The Raman shift of the 30% chromium doped a-Si thin films after annealing is shown in Figure 4. The spectral components are deconvoluted into four parts that belong to (a) amorphous silicon (468 cm^{-1}), (b) hexagonal silicon

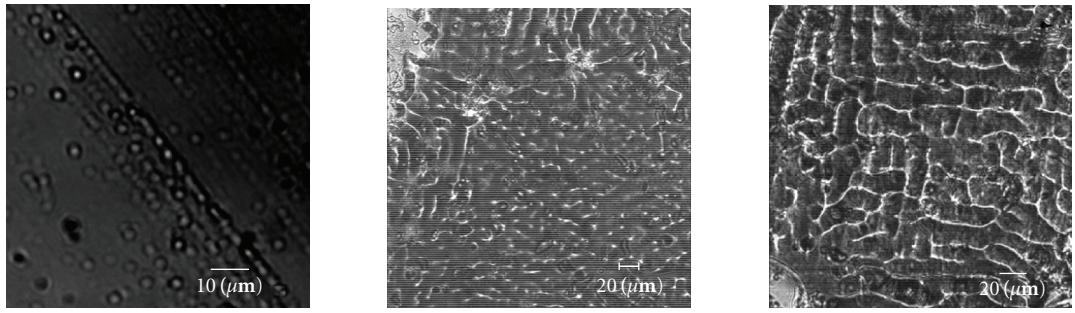

(a) (b) (c)

Figure 1: Optical micrograph of (a) a-Si thin film on BSG substrates showing shallow saucer pits (S-pits). (b) Cr/a-Si/BSG after annealing at 500°C for 20 minutes. (c) 280 nm thick a-Si film with 30 nm of Cr overlayer annealed at 500°C for 20 minutes.

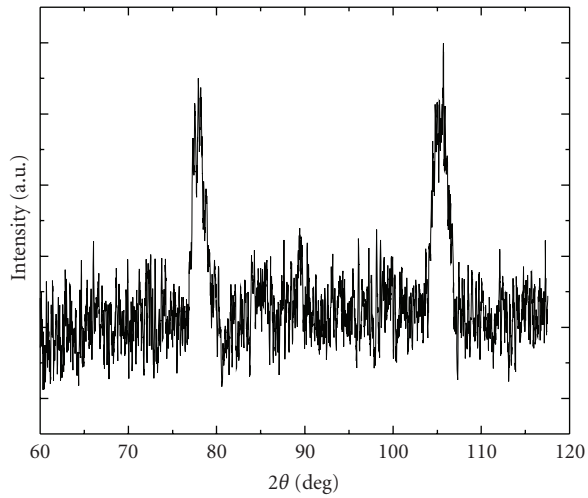

Figure 2: X-ray diffraction pattern of Cr/a-Si/BSG after annealing at 500°C for 20 minutes.

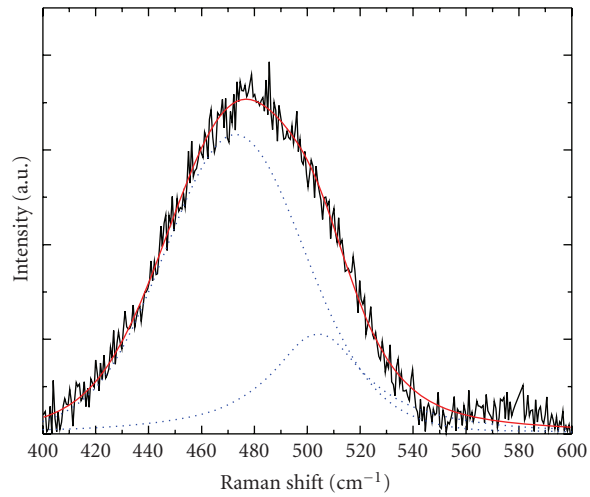

Figure 3: Raman shift of as deposited a-Si thin film on glass.

(496 cm^{-1}), (c) cubic silicon (512 cm^{-1}), and (d) Cr_2O_3 (548 cm^{-1}). Once the concentration of Cr was decreased to 5%, the silicon started crystallizing in wurzite structure. The Raman shift of the wurzite silicon is shown in Figure 5. The presence of the wurtzite structure, in the current case, is confirmed by the prominent Γ_5' resonance peak at 496 cm^{-1}. However, the theoretically predicted resonance peak is at 498 cm^{-1} [25]. The downward shift of 2 cm^{-1} can be attributed to the strain or small crystallite size of wurzite silicon. The peak at 548 cm^{-1} belongs to Cr_2O_3 (Oxide formation is not avoidable in a furnace working in ambient atmosphere). Metal silicide ($CrSi_2$) peaks at 307 and 350 cm^{-1} are also observed in the low-frequency part of the Raman spectra shown in the inset of Figure 4. The presence of Cr_2O_3, from the Raman spectra, indicates surface oxidation of the films. This would also suggest the possibility of some SiO_x phase being present in the films. However, it is difficult to unambiguously establish this since the thin films are grown on borosilicate glass substrates. Similarly, distinguishing SiO_x from films and substrate would be difficult using FTIR. Hence, while the presence of SiO_x in the films cannot be ruled out, its presence cannot also be unambiguously established in the current case.

Wurzite silicon has three vibrational peaks corresponding to the two vibrations in the plane of hexagonal layers and one perpendicular to these layers [25]. Zhang et al. have reported wurzite silicon by laser ablation [26], and they observed Raman peaks at 516 and 518 cm^{-1} due to the hexagonal silicon. In contrast, our investigations indicate that the Si films crystallize in the mixed structure at high Cr concentrations and in the wurzite structure at low Cr concentrations. A survey of the structures of Cr_2O_3 and $CrSi_2$ reveals that Cr_2O_3 exists in the corundum structure with a space group R $\bar{3}$ c with six formula units in the hexagonal unit cell. The metal ions are located in special positions along the threefold axis at ±[0 0 z; 0 0 (1/2) +z] and the oxygens lie on diads at ±[x 0 (1/4); 0 x (1/4); (1/4)] [27] and in the case of $CrSi_2$, they have three formula units per hexagonal unit cell. Its lattice parameters are a = 4.431 Å and c = 6.354 Å [28]. It is, therefore, clear that the silicide and the oxide both exist in the hexagonal form and are structurally isomorphous to the hexagonal form of Si. As a consequence, they act as

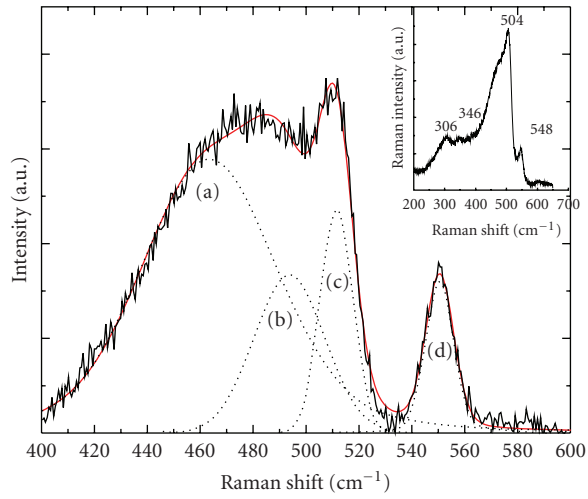

Figure 4: The Raman spectral components are deconvoluted into four parts that belong to (a) amorphous Silicon, (b) hexagonal Silicon, (c) cubic Silicon, and (d) Cr_2O_3.

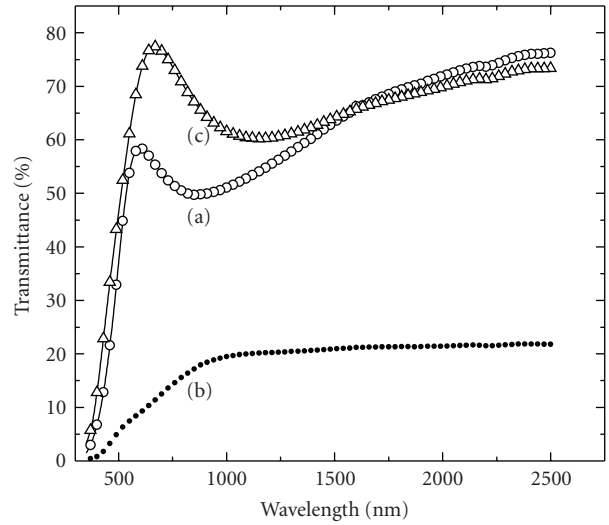

Figure 6: The spectral transmittance of the (a) 100 nm pure a-Si thin film, (b) a-Si film with a 30 nm Cr thin film blanket, and (c) after annealing at 500°C for 20 minutes.

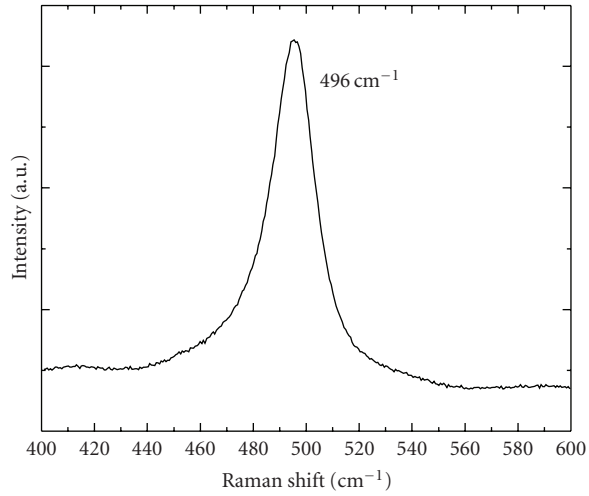

Figure 5: The Raman shift of the wurzite silicon centered at 496 cm^{-1} due to Γ_5' resonances.

seeds for the formation of the hexagonal-wurtzite structure of silicon in the crystallization process. To the best of our knowledge, this is the first experimental evidence of metal-induced wurzite structure crystallization of Si.

3.3. Optical properties

The spectral transmittance of the 100 nm pure a-Si thin film is shown in Figure 6(a). The spectral transmittance of this film with a 30 nm Cr thin film blanket is shown in Figure 6(b) and the stack of these films after annealing at 500°C for 20 minutes is shown in Figure 6(c). The lower transmittance prior to annealing is due to the blanket of Cr metal film on top of the a-Si. After annealing, the increase in the transmittance, to 80%, is a combined effect of formation of different phases in the Cr/a-Si stack. It may be noted that Raman spectroscopy revealed the presence of Cr_2O_3, after annealing in ambient atmosphere. Apart from these oxide compounds the formation of $CrSi_2$was also in evidence. $CrSi_2$is intrinsically a semiconductor with a band gap of 0.35 eV [28], but the observed absorption edge as estimated from the value at which the spectral transmittance falls to 20% is much higher. The actual calculated values are discussed below. From the spectral transmittance curves another important optical property, refractive index, can also be extracted. The index of refraction is sensitive to the coordination chemistry and composition around Si. In the present study, as mentioned earlier, after annealing, different compounds with varying concentrations are found in the volume of the sample and also on the surface. This has immense effect on the thin film refractive index. The refractive index behaviour before (*open circles*) and after annealing (*closed circles*), as function of wavelength, in Figure 7 shows that the values varied from 2.7 to 2.5 at 1100 nm of wavelength for the film of thickness 100 nm whereas the bulk silicon value is 3.4.

The optical band gap (Tauc gap) is determined from the extrapolation of linear part in the $(\alpha h\upsilon)^{1/2}$ Vs $h\upsilon$ plot assuming an indirect band gap. The band gap variation with the thickness of the a-Si thin films before and after annealing is shown in Figure 8. It is observed that the band gap varied from 2 eV for the 100 nm thick film to 1.3 eV for the film of thickness 600 nm. It is interesting that the optical absorption edge of the as-deposited a-Si thin film and the film after annealing with a 30 nm Cr layer on the top remained unaltered. The edge, in contrast, shifted towards lower energies for the Cr/a-Si/BSG stack before annealing. This small red shift in the absorption edge could be due to the formation of metal silicide during deposition. The absorption edge, which represents the electronic band structure of the materials, remained almost unaltered after annealing.

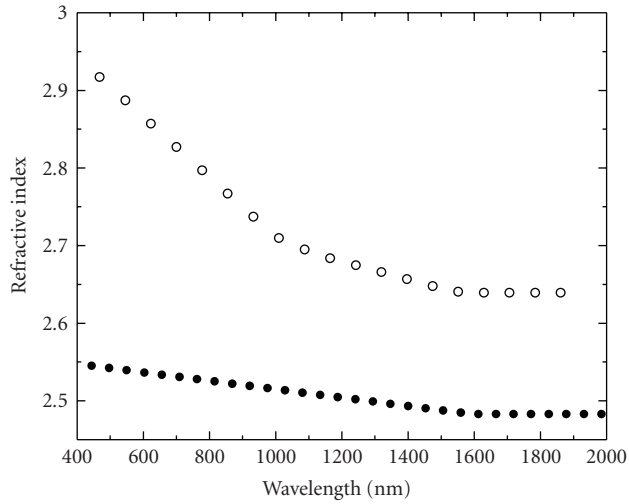

FIGURE 7: The refractive index behaviour of a 100 nm Si thin film as function of wavelength; open circles represent pure a-Si thin film and closed circles represent the annealed film with a 30 nm Cr thin film blanket.

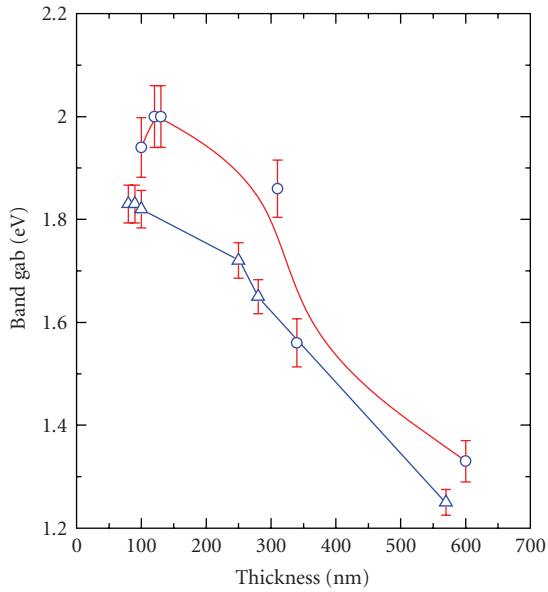

FIGURE 8: The band gap variation as function of thickness for the (open triangles) as deposited pure a-Si films (closed circles) after annealing.

This signifies the fact that the different compounds observed during the annealing process do not disturb or affect the essential optical properties of a-Si. We believe this to be a very important observation for several optical applications relying on nanocrystalline-Si.

4. CONCLUSIONS

The stabilization of wurtzite structure of silicon via metal-induced nanocrystallization is demonstrated. The identification of the crystalline phase was done using Raman spectroscopy and x-ray diffraction. The optical properties of the nanocrystalline silicon thin films are characterized by high transmittance, a lower refractive index than bulk diamond-like Si but a larger optical band gap. The presence of $CrSi_2$ and Cr_2O_3 seems to trigger the formation of the wurtzite structure.

ACKNOWLEDGMENTS

The authors acknowledge the financial support from the DST-ITPAR Program. K. U. M. Kumar would like to thank the DST-ITPAR for providing a Bose-Romagnosi fellowship to do this work. Facilities provided by the UGC under UPE and SAP Programs are gratefully acknowledged. The authors wish to thank Dr. Vasant Sathe, UGC-DAE CSR, Indore centre, for the invaluable help in Raman spectroscopy measurements.

REFERENCES

[1] J. Huo, R. Solanki, J. L. Freeouf, and J. R. Carruthers, "Electroluminescence from silicon nanowires," *Nanotechnology*, vol. 15, no. 12, pp. 1848–1850, 2004.

[2] W. Jantsch, S. Lanzerstorfer, L. Palmetshofer, M. Stepikhova, and H. Preier, "Different Er centres in Si and their use for electroluminescent devices," *Journal of Luminescence*, vol. 80, no. 1–4, pp. 9–17, 1998.

[3] T. A. Burr, A. A. Seraphin, E. Werwa, and K. D. Kolenbrander, "Carrier transport in thin films of silicon nanoparticles," *Physical Review B*, vol. 56, no. 8, pp. 4818–4824, 1997.

[4] N. Koshida, T. Ohta, and B. Gelloz, "Operation of nanosilicon ballistic electron emitter in liquid water and hydrogen generation effect," *Applied Physics Letters*, vol. 90, no. 16, Article ID 163505, 2007.

[5] H. Shinoda, T. Nakajima, K. Ueno, and N. Koshida, "Thermally induced ultrasonic emission from porous silicon," *Nature*, vol. 400, no. 6747, pp. 853–855, 1999.

[6] W. Sun, J. E. Puzas, T.-J. Sheu, and P. M. Fauchet, "Porous silicon as a cell interface for bone tissue engineering," *Physica Status Solidi (A)*, vol. 204, no. 5, pp. 1429–1433, 2007.

[7] S. Holgado, J. Martínez, J. Garrido, C. Morant, and J. Piqueras, "Rapid solid phase crystallization of nanocrystalline silicon deposited by electron cyclotron plasma chemical vapor deposition," *Applied Physics Letters*, vol. 69, no. 13, pp. 1873–1875, 1996.

[8] J. C. Bean, H. J. Leamy, J. M. Poate, et al., "Epitaxial laser crystallization of thin-film amorphous silicon," *Applied Physics Letters*, vol. 33, no. 3, pp. 227–230, 1978.

[9] K. U. M. Kumar, R. Brahma, M. G. Krishna, A. K. Bhatnagar, and G. Dalba, "An optical study of Ni induced crystallization of a-Si thin films," *Journal of Physics: Condensed Matter*, vol. 19, no. 49, Article ID 496208, 11 pages, 2007.

[10] J. Bandet, B. Despax, and M. Caumont, "Vibrational and electronic properties of stabilized wurtzite-like silicon," *Journal of Physics D*, vol. 35, no. 3, pp. 234–239, 2002.

[11] J.-H. Shim, S. Im, Y. J. Kim, and N.-H. Cho, "Nanostructural and optical features of hydrogenated nanocrystalline silicon films prepared by aluminium-induced crystallization," *Thin Solid Films*, vol. 503, no. 1-2, pp. 55–59, 2006.

[12] L. R. Muniz, C. T. M. Ribeiro, A. R. Zanatta, and I. Chambouleyron, "Aluminium-induced nanocrystalline Ge formation at low temperatures," *Journal of Physics: Condensed Matter*, vol. 19, no. 7, 2007.

[13] C. Hayzelden and J. L. Batstone, "Silicide formation and silicide-mediated crystallization of nickel-implanted amorphous silicon thin films," *Journal of Applied Physics*, vol. 73, no. 12, pp. 8279–8289, 1993.

[14] A. F. Wells, *Structural Inorganic Chemistry*, Oxford University Press, Oxford, UK, 4th edition, 1975.

[15] E. G. Birgin, I. Chambouleyron, and J. M. Martínez, "Estimation of the optical constants and the thickness of thin films using unconstrained optimization," *Journal of Computational Physics*, vol. 151, no. 2, pp. 862–880, 1999.

[16] D. Pomerantz, "A cause and cure of stacking faults in silicon epitaxial layers," *Journal of Applied Physics*, vol. 38, no. 13, pp. 5020–5026, 1967.

[17] C. W. Pearce and R. G. McMahon, "Role of metallic contamination in the formation of "saucer" pit defects in epitaxial silicon," *Journal of Vacuum Science and Technology*, vol. 14, no. 1, pp. 40–43, 1977.

[18] J. H. Choi, D. Y. Kim, S. S. Kim, S. J. Park, and J. Jang, "Polycrystalline silicon prepared by metal induced crystallization," *Thin Solid Films*, vol. 440, no. 1-2, pp. 1–4, 2003.

[19] S. Y. Yoon, S. J. Park, K. H. Kim, and J. Jang, "Metal-induced crystallization of amorphous silicon," *Thin Solid Films*, vol. 383, no. 1-2, pp. 34–38, 2001.

[20] B. G. Yacobi, A. J. Szadkowski, S. Zukotynski, and J. M. Corbett, "Compound formation between amorphous silicon and chromium," *Journal of Applied Physics*, vol. 51, no. 12, pp. 6424–6425, 1980.

[21] J. S. Preston, H. M. van Driel, and J. E. Sipe, "Order-disorder transitions in the melt morphology of laser-irradiated silicon," *Physical Review Letters*, vol. 58, no. 1, pp. 69–72, 1987.

[22] M. A. Bösch and R. A. Lemons, "Laser-induced melt dynamics of Si and silica," *Physical Review Letters*, vol. 47, no. 16, pp. 1151–1155, 1981.

[23] L. M. Levinson, "Highly anisotropic columnar structures in silicon," *Applied Physics Letters*, vol. 21, no. 6, pp. 289–291, 1972.

[24] J. Zi, H. Buscher, C. Falter, W. Ludwig, K. Zhang, and X. Xie, "Raman shifts in Si nanocrystals," *Applied Physics Letters*, vol. 69, no. 2, pp. 200–202, 1996.

[25] R. J. Kobliska and S. A. Solin, "Raman spectrum of wurtzite silicon," *Physical Review B*, vol. 8, no. 8, pp. 3799–3802, 1973.

[26] Y. Zhang, Z. Iqbal, S. Vijayalakshmi, and H. Grebel, "Stable hexagonal-wurtzite silicon phase by laser ablation," *Applied Physics Letters*, vol. 75, no. 18, pp. 2758–2760, 1999.

[27] R. E. Newnham and Y. M. Dehaan, "Refinement of the a A1203, Ti203, V203 and Cr203 structures," *Zeitschrift für Kristallographie: New Crystal Structures*, vol. 117, p. 235, 1962.

[28] M. C. Bost and J. E. Mahan, "An investigation of the optical constants and band gap of chromium disilicide," *Journal of Applied Physics*, vol. 63, no. 3, pp. 839–844, 1988.

Hindawi Publishing Corporation
Journal of Nanomaterials
Volume 2008, Article ID 156724, 5 pages
doi:10.1155/2008/156724

Research Article

Thermomechanical Stresses in Fullerenes at Nanotube

Nicola M. Pugno

Dipartimento di Ingegneria Strutturale e Geotecnica, Politecnico di Torino, Corso Duca degli Abruzzi 24, 10129 Torino, Italy

Correspondence should be addressed to Nicola M. Pugno, nicola.pugno@polito.it

Received 25 November 2007; Accepted 13 March 2008

Recommended by Robert Dorey

The thermomechanical stresses acting between a nanotube and fullerenes encapsulated on it are computed. After a general formulation, based on elasticity, we have applied the analysis to C82@(10,10) or C60@(10,10) peapods finding stresses in the gigapascal range or vanishing, respectively. The analysis suggests that a thermal control could be used to produce smart fullerenes at nanotube systems, for example, as two-stage nanovectors for drug delivery.

1. INTRODUCTION

The Royal Swedish Academy of Sciences awarded the 1996 Nobel Prize in Chemistry jointly to Curl, Kroto, and Smalley for their discovery in 1985, together with Heath and O'Brien [1], of fullerenes. It is common belief that the discovery of carbon nanotubes (CNTs) took place in 1991 thanks to Iijima [2], who reported in *Nature* the observation of multiwalled CNTs. In 1993, in the same issue of *Nature*, two independent groups, again Iijima with Ichihashi [3] and Bethune et al. [4], reported the observation of single-walled CNTs. The impact of these papers on the scientific community has been unquestionably tremendous. In spite of this, the first direct observation of a multiwalled CNT (by force subsequent to the production of the transmission electron microscope) was previously reported in 1952 in the Journal of Physical Chemistry of Russia by Radushkevich and Lukyanovich [5], whereas an image, even if controversial, of a single- (or possibly double-) walled CNT was reported in 1976 by Oberlin el al. in the Journal of Crystal Growth [6]. Two editorials, appearing in Carbon in 1997 [7] and 2006 [8], support these pioneering observations.

Aside from the controversy surrounding the discovery of nanotubes, fullerenes and nanotubes have introduced humanity to the new nanoera. In particular, the giant strength and Young's modulus of carbon fullerenes and nanotubes, combined with a low density, promise to revolutionize materials science, as required in the design of super-strong space elevator megacables [9] or super-adhesive Spiderman suits [10]. Combining the two nanostructures even more intriguing systems could be realized.

In this paper, we analyze the thermomechanical stresses acting between a nanotube and encapsulated fullerenes (e.g., see [11, 12]). We have solved the problem treating the fullerenes as a fluid inside an elastic channel (nanotube). We have applied the analysis to a C82@(10,10) system finding huge thermomechanical stresses, in the gigapascal range. A C60@(10,10) system is also considered for comparison and is found free of stresses. Thus the analysis suggests that a thermal control could be used to produce smart fullerenes at nanotube systems, for example, as two-stage nanovectors for drug delivery.

2. THE THERMOMECHANICAL ELASTIC MODEL

Consider a nanotube filled by fullerenes (Figure 1). After a temperature variation, the nanotube diameter will change, interacting with the fullerenes. We treat the nanotube as an elastic cylindrical shell and the fullerenes as elastic spheres. We assume a constant pressure distribution between nanotube and fullerenes, due to the small spacing between fullerenes (0.34 nm), so that their action on the nanotube can be considered as a distributed pressure, for example, as a fluid inside an elastic channel.

Let us consider a linear elastic isotropic sphere of inner and outer radii a and b subjected to inner and outer pressures

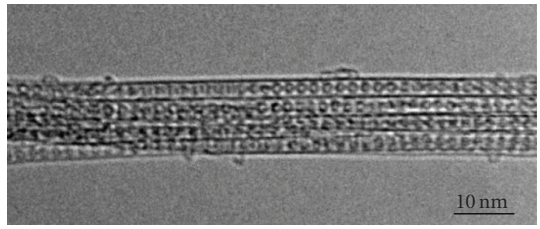

Figure 1: Example of fullerenes at nanotubes (Courtesy of Chiu Po-Wen).

p and q, respectively. The radial σ_r and circumferential σ_ϑ stressesat a generic radius $a < r < b$ are [13]

$$\sigma_r = \frac{1}{b^3 - a^3}\left(- b^3 q + a^3 p + \frac{a^3 b^3}{r^3}(q - p)\right),$$
$$\sigma_\vartheta = \frac{1}{b^3 - a^3}\left(- b^3 q + a^3 p - \frac{a^3 b^3}{2r^3}(q - p)\right). \quad (1)$$

Linear elastic isotropic laws for spherical symmetry become

$$\varepsilon_r \equiv \frac{\mathrm{d}u}{\mathrm{d}r} = \frac{\sigma_r}{E} - \frac{2\nu}{E}\sigma_\vartheta, \qquad \varepsilon_\vartheta \equiv \frac{u}{r} = \frac{\sigma_\vartheta}{E} - \frac{\nu}{E}(\sigma_\vartheta + \sigma_r), \quad (2)$$

where E and ν are the Young modulus and Poisson ratio of the material and u is the radial elastic displacement (along r). We will apply (1) and (2) to fullerenes, thus considering them as elastic spheres.

Analogously, let us consider a linear elastic isotropic cylinder (of length L) of inner and outer radii a and b subjected to inner and outer pressures p and q, respectively. The radial and circumferential stresses at a generic radius $a < r < b$ are [13]

$$\sigma_r = \frac{1}{b^2 - a^2}\left(- b^2 q + a^2 p + \frac{a^2 b^2}{r^2}(q - p)\right),$$
$$\sigma_\vartheta = \frac{1}{b^2 - a^2}\left(- b^2 q + a^2 p - \frac{a^2 b^2}{r^2}(q - p)\right). \quad (3)$$

Linear elastic isotropic laws for cylindrical symmetry become

$$\varepsilon_r \equiv \frac{\mathrm{d}u}{\mathrm{d}r} = \frac{\sigma_r}{E'} - \frac{\nu'}{E'}\sigma_\vartheta, \qquad \varepsilon_\vartheta \equiv \frac{u}{r} = \frac{\sigma_\vartheta}{E'} - \frac{\nu'}{E'}\sigma_r,$$
$$E' = E, \quad \nu' = \nu \text{ for plane stress;}$$
$$E' = \frac{E}{1 - \nu^2}, \quad \nu' = \frac{\nu}{1 - \nu} \text{ for plane strain.} \quad (4)$$

We can assume plain stress condition (i.e., $\sigma_z = 0$) or plane strain condition (i.e., $\varepsilon_z = 0$, for which in addition $\sigma_z = \nu(\sigma_r + \sigma_\vartheta)$). Assuming a nanotube with free ends, the first case is the most realistic, whereas the second case better describes fixed ends; thus we will treat nanotubes as elastic cylinders, by (3) and (4).

Consider a single fullerene at temperature T as a linear elastic isotropic sphere (elastic properties with subscript "f") having inner and outer radii r_i and r_o, respectively. The confinement from the nanotube is described by the external pressure p. According to (1) and (2)

$$\sigma_r(r) = -\frac{1 - r_i^3/r^3}{1 - r_i^3/r_o^3}p,$$
$$\sigma_\vartheta(r) = -\frac{1 + r_i^3/2r^3}{1 - r_i^3/r_o^3}p,$$
$$u_{\mathrm{tot}}(r) = u(r) + \alpha_f(T)\Delta T r$$
$$= \left[\frac{\sigma_\vartheta(r)}{E_f} - \frac{\nu_f}{E_f}(\sigma_\vartheta(r) + \sigma_r(r)) + \alpha_f(T)\Delta T\right]r, \quad (5)$$

where u_{tot} is the total (elastic + thermal) radial displacement, α_f is the thermal expansion coefficient for fullerene (in general a function of the temperature, see Section 3), and ΔT is the temperature variation.

Thus the fullerene elastic outer radius r_o^* (r_o if unstressed) is

$$r_o^* = r_o + u_{\mathrm{tot}}(r = r_o). \quad (6)$$

Now consider a nanotube at temperature T as a linear elastic isotropic cylinder (elastic properties with subscript "n") having inner and outer radii R_i and R_o, respectively. The confinement from the fullerenes is described by the internal pressure p. According to (3) and (4):

$$\sigma_r(r) = \frac{R_i^2/R_o^2 - R_i^2/r^2}{1 - R_i^2/R_o^2}p, \qquad \sigma_\vartheta(r) = \frac{R_i^2/R_o^2 + R_i^2/r^2}{1 - R_i^2/R_o^2}p, \quad (7)$$

$$u_{\mathrm{tot}}(r) = u(r) + \alpha_n(T)\Delta T r = \left[\frac{\sigma_\vartheta(r)}{E_n'} - \frac{\nu_n'}{E_n'}\sigma_r(r) + \alpha_n(T)\Delta T\right]r. \quad (8)$$

Thus the nanotube elastic inner radius R_i^* (R_i if unstressed) is

$$R_i^* = R_i + u_{\mathrm{tot}}(r = R_i). \quad (9)$$

The compatibility of the displacements (elastic contact between nanotube and fullerenes) implies

$$r_o^*(p, \Delta T) = R_i^*(p, \Delta T). \quad (10)$$

The solution of (10) gives the effective internal pressure p^*; the fullerenes/nanotube internal/external radius as a function of temperature are simply given by $r_i^*(p^*, \Delta T) = r_o^*(p^*, \Delta T) - tR_o^*(p^*, \Delta T) = R_i^*(p^*, \Delta T) + t$, where t is the shell thickness (0.34 nm); moreover, $r_0^*(p^*, \Delta T) = R_i^*(p^*, \Delta T)$ can be derived from (9). From the computed

Table 1: Computed values for C60@(10,10), thermomechanical stresses are vanishing.

T [K]	α_f [K^{-1}]	α_n [K^{-1}]	r_o' [nm]	R_i' [nm]	r_o^* [nm]	R_i^* [nm]
290	0.000006	−0.000009	0.500000	0.530000	0.500000	0.530000
280	0.000005	−0.000008	0.499973	0.530045	0.499973	0.530045
270	0.000005	−0.000008	0.499950	0.530086	0.499950	0.530086
260	0.000005	−0.000008	0.499931	0.530124	0.499931	0.530124
250	0.000004	−0.000008	0.499917	0.530159	0.499917	0.530159
240	0.000004	−0.000007	0.499906	0.530191	0.499906	0.530191
230	0.000003	−0.000007	0.499900	0.530219	0.499900	0.530219
220	0.000003	−0.000007	0.499898	0.530245	0.499898	0.530245
210	0.000003	−0.000006	0.499900	0.530267	0.499900	0.530267
200	0.000002	−0.000006	0.499906	0.530286	0.499906	0.530286
190	0.000002	−0.000006	0.499917	0.530302	0.499917	0.530302
180	0.000001	−0.000005	0.499931	0.530315	0.499931	0.530315
170	0.000001	−0.000005	0.499950	0.530324	0.499950	0.530324
160	0.000000	−0.000005	0.499973	0.530331	0.499973	0.530331
150	0.000000	−0.000005	0.500000	0.530334	0.500000	0.530334
140	0.000000	−0.000004	0.500031	0.530334	0.500031	0.530334
130	−0.000001	−0.000004	0.500067	0.530331	0.500067	0.530331
120	−0.000001	−0.000004	0.500106	0.530324	0.500106	0.530324
110	−0.000002	−0.000003	0.500150	0.530315	0.500150	0.530315
100	−0.000002	−0.000003	0.500198	0.530302	0.500198	0.530302
90	−0.000003	−0.000003	0.500250	0.530286	0.500250	0.530286
80	−0.000003	−0.000002	0.500306	0.530267	0.500306	0.530267
70	−0.000003	−0.000002	0.500367	0.530245	0.500367	0.530245
60	−0.000003	−0.000002	0.500329	0.530219	0.500329	0.530219
50	−0.000002	−0.000002	0.500286	0.530191	0.500286	0.530191
40	−0.000002	−0.000001	0.500238	0.530159	0.500238	0.530159
30	−0.000001	−0.000001	0.500186	0.530124	0.500186	0.530124
20	−0.000001	−0.000001	0.500129	0.530086	0.500129	0.530086
10	0.000000	0.000000	0.500067	0.530045	0.500067	0.530045

value of the pressure p^* the thermomechanical stresses and strains in the fullerenes and nanotubes can be calculated via (1)–(4).

3. APPLICATION TO THE C82(10,10) OR C60(10,10) PEAPODS

According to the previous analysis, we consider nanotube or fullerenes as elastic cylindrical or spherical thin shells; we assume a constant thickness t and plane stress condition and both nanotube and fullerenes composed by the same material, for which we assume $E_f = E_n = E \approx 1\,\text{TPa}$, $\nu_f = \nu_n = \nu \approx 0$ (carbon). For an (n,m) nanotube and for Cl fullerenes, the mean radii (at room temperature, i.e., at 290 K) are respectively given by

$$R_n = \frac{R_o + R_i}{2} \approx 0.0392\sqrt{n^2 + m^2 + nm}\ \text{nm},$$
$$R_f = r = \frac{r_o + r_i}{2} \approx 0.0458\sqrt{l}\ \text{nm}, \tag{11}$$

so that $R_i = R_n - t/2$ and $r_o = R_f + t/2$ with $t = 0.3$ nm (close to the van der Waals spacing [14]). For $r_o > R_i$ mechanical stresses will be present.

In addition, the thermal volumetric expansion coefficient β_f of carbon fullerenes is [15]

$$\beta_f \approx 3\alpha_f(T) \approx \begin{cases} -1 \times 10^{-5}\dfrac{T}{70} & T < 70\,\text{K}, \\ 1 \times 10^{-5}\dfrac{T - 150}{80} & 70\,\text{K} \le T < 400\,\text{K}, \end{cases} \tag{12}$$

which thus changes sign around 70 K, whereas the thermal expansion coefficient of a carbon nanotube, according to [15], is always negative in the considered temperature range:

$$\alpha_n \approx -1.2 \times 10^{-5}\frac{T}{400} \quad T < 400\,\text{K}. \tag{13}$$

Table 2: Computed values for C82@(10,10), thermomechanical stresses are in the gigapascal range.

T [K]	r_o' [nm]	R_i' [nm]	p [MPa]	σ_{rf}, σ_{rn} [MPa]	$\sigma_{\vartheta f}$ [MPa]	$\sigma_{\vartheta n}$ [MPa]	r_o^* [nm]	R_i^* [nm]
290	0.56000	0.53000	18939.39	−18939.39	−12941.92	42929.29	0.55469	0.55919
280	0.55997	0.53004	18892.14	−18892.14	−12909.63	42822.18	0.55468	0.55916
270	0.55994	0.53009	18849.84	−18849.84	−12880.72	42726.29	0.55466	0.55914
260	0.55992	0.53012	18812.49	−18812.49	−12855.20	42641.64	0.55465	0.55912
250	0.55991	0.53016	18780.09	−18780.09	−12833.06	42568.21	0.55465	0.55911
240	0.55990	0.53019	18752.65	−18752.65	−12814.31	42506.01	0.55464	0.55909
230	0.55989	0.53022	18730.16	−18730.16	−12798.95	42455.04	0.55464	0.55909
220	0.55989	0.53024	18712.63	−18712.63	−12786.96	42415.30	0.55464	0.55909
210	0.55989	0.53027	18700.05	−18700.05	−12778.37	42386.78	0.55465	0.55909
200	0.55990	0.53029	18692.42	−18692.42	−12773.16	42369.49	0.55466	0.55910
190	0.55991	0.53030	18689.75	−18689.75	−12771.33	42363.44	0.55467	0.55911
180	0.55992	0.53031	18692.03	−18692.03	−12772.89	42368.61	0.55469	0.55913
170	0.55994	0.53032	18699.27	−18699.27	−12777.83	42385.01	0.55471	0.55915
160	0.55997	0.53033	18711.46	−18711.46	−12786.16	42412.63	0.55473	0.55917
150	0.56000	0.53033	18728.60	−18728.60	−12797.88	42451.49	0.55475	0.55920
140	0.56004	0.53033	18750.69	−18750.69	−12812.97	42501.57	0.55478	0.55923
130	0.56007	0.53033	18777.74	−18777.74	−12831.46	42562.89	0.55481	0.55927
120	0.56012	0.53032	18809.75	−18809.75	−12853.33	42635.43	0.55485	0.55932
110	0.56017	0.53031	18846.70	−18846.70	−12878.58	42719.20	0.55489	0.55936
100	0.56022	0.53030	18888.62	−18888.62	−12907.22	42814.19	0.55493	0.55942
90	0.56028	0.53029	18935.48	−18935.48	−12939.24	42920.42	0.55497	0.55947
80	0.56034	0.53027	18987.30	−18987.30	−12974.65	43037.88	0.55502	0.55953
70	0.56041	0.53024	19044.07	−19044.07	−13013.45	43166.56	0.55508	0.55960
60	0.56037	0.53022	19033.19	−19033.19	−13006.02	43141.91	0.55504	0.55956
50	0.56032	0.53019	19020.96	−19020.96	−12997.66	43114.18	0.55499	0.55951
40	0.56027	0.53016	19007.37	−19007.37	−12988.37	43083.36	0.55494	0.55946
30	0.56021	0.53012	18992.41	−18992.41	−12978.15	43049.47	0.55489	0.55940
20	0.56014	0.53009	18976.10	−18976.10	−12967.00	43012.49	0.55483	0.55933
10	0.56007	0.53004	18958.43	−18958.43	−12954.92	42972.43	0.55476	0.55927

Thus, according to these numerical solutions, following the analysis reported in Section 2, we derive

$$p = p^* = \begin{cases} E\dfrac{(R_f + t/2)(1+\alpha_f \Delta T) - (R_n - t/2)(1+\alpha_n \Delta T)}{R_n/t(R_n - t/2) + R_f/(2t)(R_f + t/2)} = \chi & \\ \qquad\qquad \text{if } \chi > 0 \text{ (contact)}, & \\ 0 \qquad\qquad \text{if } \chi \le 0 \text{ (no contact)}, & \end{cases}$$

$$\sigma_{rf,n}^{(\max)} = -p, \quad \sigma_{\vartheta f} = -\frac{R_f}{2t}p, \quad \sigma_{\vartheta n} = \frac{R_n}{t}p,$$

$$R_{f,n}^* = R_{f,n}\left(1 + \frac{\sigma_{\vartheta f,n}}{E} + \alpha_{f,n}\Delta T\right),$$

$$R_{f,n}' = R_{f,n}(1 + \alpha_{f,n}\Delta T), \tag{14}$$

where $\sigma_r^{(\max)}$ is the maximum radial stress, thus evaluated at r_o and R_i (at r_i and R_o we have $\sigma_r = 0$) and $R_{f,n}'$ are the radii of the nanotube and fullerenes if assumed to be not interacting.

The cases of a (10,10) nanotube ($R_n \approx 0.68$ nm) coupled with C60 ($R_f \approx 0.35$ nm) or C82 ($R_f \approx 0.41$ nm) fullerenes cooled from 290 K to 10 K are reported in Tables 1 and 2, respectively. Note that the diameter variation is very small, but stresses are huge for C82@(10,10), in the gigapascale range, but are vanishing for the C60@(10,10) peapod. Note the maximum circumferential tensile stress in the nanotube around 70 K of 43 GPa, whereas the circumferential compression in the fullerenes is of 13 GPa; the calculated contact pressure is of 19 GPa.

Considering different elastic constants (E, ν) would correspond to slightly different values, whereas the thermal expansion coefficients and in general the radii, unfortunately not fully defined for an atomistic object (see (8) and (11)), play a dramatic role on the computed thermomechanical stresses. Thus the analysis is accurate in the procedure but the deduced thermal stresses must be viewed just as an example of calculation. Slightly changing the definition of the radii (e.g., considering a different value for t) we have found an intermediate behaviour in which the interaction fullerenes-nanotube vanishes only in a given temperature range. This suggests that fullerenes (other types of nanoparticles can

be envisioned too) could be released from the nanotube by thermal activation, a perhaps useful concept for producing innovative two-stage nanovectors capable of smartly delivering the fullerenes/drugs by a remote thermal control.

4. CONCLUSIONS

According to our analysis, the thermomechanical stresses of a fullerenes at nanotube peapod can be tuned by varying the temperature in a controllable way. Tunable stiffness and band structure (metallic, semiconductor) of a nanotube could thus be achieved by embedding fullerenes on it and by controlling the temperature. The analysis suggests that smart fullerenes at nanotube peapods, such as two-stage nanovectors for drug delivery, could in principle be realized by remote thermal activation.

ACKNOWLEDGMENT

The author is supported by the "Bando Ricerca Scientifica Piemonte BIADS 2006": novel biomaterials for intraoperative adjustable devices for fine tuning of prostheses shape and performance in surgery.

REFERENCES

[1] H. W. Kroto, J. R. Heath, S. C. O'Brien, R. F. Curl, and R. E. Smalley, "C_{60}: buckminsterfullerene," *Nature*, vol. 318, no. 6042, pp. 162–163, 1985.

[2] S. Iijima, "Helical microtubules of graphite carbon," *Nature*, vol. 354, no. 6348, pp. 56–58, 1991.

[3] S. Iijima and T. Ichihashi, "Single-shell carbon nanotubes of 1-nm diameter," *Nature*, vol. 363, no. 6430, pp. 603–605, 1993.

[4] D. S. Bethune, C. H. Klang, M. S. de Vries, et al., "Cobalt-catalysed growth of carbon nanotubes with single-atomic-layer walls," *Nature*, vol. 363, no. 6430, pp. 605–607, 1993.

[5] L. V. Radushkevich and V. M. Lukyanovich, "O strukture ugleroda, obrazujucegosja pri termiceskom razlozenii okisi ugleroda na zeleznom kontakte," *Zurn Fisic Chim*, vol. 26, pp. 88–95, 1952.

[6] A. Oberlin, M. Endo, and T. Koyama, "Filamentous growth of carbon through benzene decomposition," *Journal of Crystal Growth*, vol. 32, no. 3, pp. 335–349, 1976.

[7] H. P. Boehm, "The first observation of carbon nanotubes," *Carbon*, vol. 35, no. 4, pp. 581–584, 1997.

[8] M. Monthioux and V. L. Kuznetsov, "Who should be given the credit for the discovery of carbon nanotubes?" *Carbon*, vol. 44, no. 9, pp. 1621–1624, 2006.

[9] N. M. Pugno, "The role of defects in the design of space elevator cable: from nanotube to megatube," *Acta Materialia*, vol. 55, no. 15, pp. 5269–5279, 2007.

[10] N. M. Pugno, "Towards a Spiderman suit: large invisible cables and self-cleaning releasable super-adhesive materials," *Journal of Physics: Condensed Matter*, vol. 19, no. 39, Article ID 395001, 17 pages, 2007.

[11] B. J. Cox, N. Thamwattana, and J. M. Hill, "Mechanics of atoms and fullerenes in single-walled carbon nanotubes. I. Acceptance and suction energies," *Proceedings of the Royal Society A*, vol. 463, no. 2078, pp. 461–476, 2007.

[12] D. Baowan, N. Thamwattana, and J. M. Hill, "Zigzag and spiral configurations for fullerenes in carbon nanotubes," *Journal of Physics A*, vol. 40, no. 27, pp. 7543–7556, 2007.

[13] J. Prescott, *Applied Elasticity*, Dover, New York, NY, USA, 1946.

[14] M. Yoon, S. Berber, and D. Tománek, "Energetics and packing of fullerenes in nanotube peapods," *Physical Review B*, vol. 71, no. 15, Article ID 155406, 4 pages, 2005.

[15] Y.-K. Kwon, S. Berber, and D. Tománek, "Thermal contraction of carbon fullerenes and nanotubes," *Physical Review Letters*, vol. 92, no. 1, Article ID 015901, 4 pages, 2004.